

1 Impaired astrocytic Ca²⁺ signalling in awake Alzheimer's disease transgenic
2 mice

3 Knut Sindre Åbjørsbråten^{1†}, Gry H. E. Syverstad Skaaraas^{2†}, Céline Cunen³, Daniel M. Bjørnstad¹,
4 Kristin M. Gullestad Binder¹, Vidar Jensen¹, Lars N.G. Nilsson⁵, Shreyas B. Rao², Wannan Tang^{1,4},
5 Gudmund Horn Hermansen³, Erlend A. Nagelhus[§], Ole Petter Ottersen⁶, Reidun Torp², Rune Enger^{1*}
6

7 ¹GliaLab at the Letten Centre, Division of Anatomy, Department of Molecular Medicine, Institute of
8 Basic Medical Sciences, University of Oslo, N-0317 Oslo, Norway

9 ²Division of Anatomy, Department of Molecular Medicine, Institute of Basic Medical Sciences,
10 University of Oslo, N-0317 Oslo, Norway

11 ³Statistics and Data Science group, Department of Mathematics, Faculty of Mathematics and Natural
12 Sciences, University of Oslo, 0316, Oslo, Norway

13 ⁴Department of Clinical and Molecular Medicine, Norwegian University of Science and Technology,
14 Trondheim, Norway

15 ⁵Department of Pharmacology, University of Oslo, N-0316 Oslo, Norway

16 ⁶Office of the President, Karolinska Institutet, Stockholm, Sweden
17
18

19 † These authors have contributed equally to this work and share first authorship

20 § Deceased

21 * Correspondence: Rune Enger, Division of Anatomy, Department of Molecular Medicine, Institute
22 of Basic Medical Sciences, University of Oslo, P.O. Box 1103 Blindern, N-0317 Oslo, Norway.
23 Email: rune.enger@medisin.uio.no.

24

25 Keywords: Alzheimer's disease, amyloid plaques, Ca²⁺ imaging, startle response, norepinephrine,
26 astrocyte

27

28 Abstract

29 Increased astrocytic Ca^{2+} signaling related to amyloid plaques has been shown in Alzheimer's disease
30 mouse models, but to date no reports have characterized behaviorally induced astrocytic Ca^{2+}
31 signalling in such mice without the confounding effects of anesthesia. Here, we employ an event-
32 based algorithm to assess astrocytic Ca^{2+} signals in the neocortex of awake-behaving tg-ArcSwe mice
33 and non-transgenic wildtype littermates while monitoring pupil responses and behavior. We
34 demonstrate an attenuated astrocytic Ca^{2+} response to locomotion and an uncoupling of pupil
35 responses and astrocytic Ca^{2+} signalling in 15-months old plaque-bearing mice. This points to a
36 potential decoupling of neuromodulatory activation and astrocytic Ca^{2+} activity, which may account
37 for some of the cognitive dysfunctions observed in Alzheimer's disease.

38

39

40

41 Introduction

42 Since astrocytic Ca^{2+} signals were first discovered in the early 1990's they have been the object of
43 numerous studies exploring their roles in brain physiology and pathophysiology. Importantly, such
44 signals have been shown to occur in response to a wide array of neurotransmitters and to trigger the
45 release of substances that affect neuronal signalling and the vasculature. A growing body of evidence
46 suggests that astrocytic Ca^{2+} signals play important roles in higher brain functions such as memory
47 formation and cortical processing, mediated in part through the neuromodulatory systems of the brain
48 (Adamsky et al. 2018; Kol et al. 2020; Poskanzer and Yuste 2016, 2011; Ye et al. 2020; Paukert et al.
49 2014).

50

51 Astrocytic Ca^{2+} signalling in an Alzheimer's disease (AD) mouse model was first described by
52 Kuchibhotla et al. 2009 (Kuchibhotla et al. 2009), who found pathological Ca^{2+} waves originating at
53 amyloid plaques, and a general increase in astrocytic Ca^{2+} signalling. Later, Delekate et al. showed
54 plaque-associated astrocytic hyperactivity mediated through activation of metabotropic purine
55 receptors (Delekate et al. 2014). These studies were performed under anesthesia, which severely
56 attenuates physiological Ca^{2+} signals (Thrane et al. 2012).

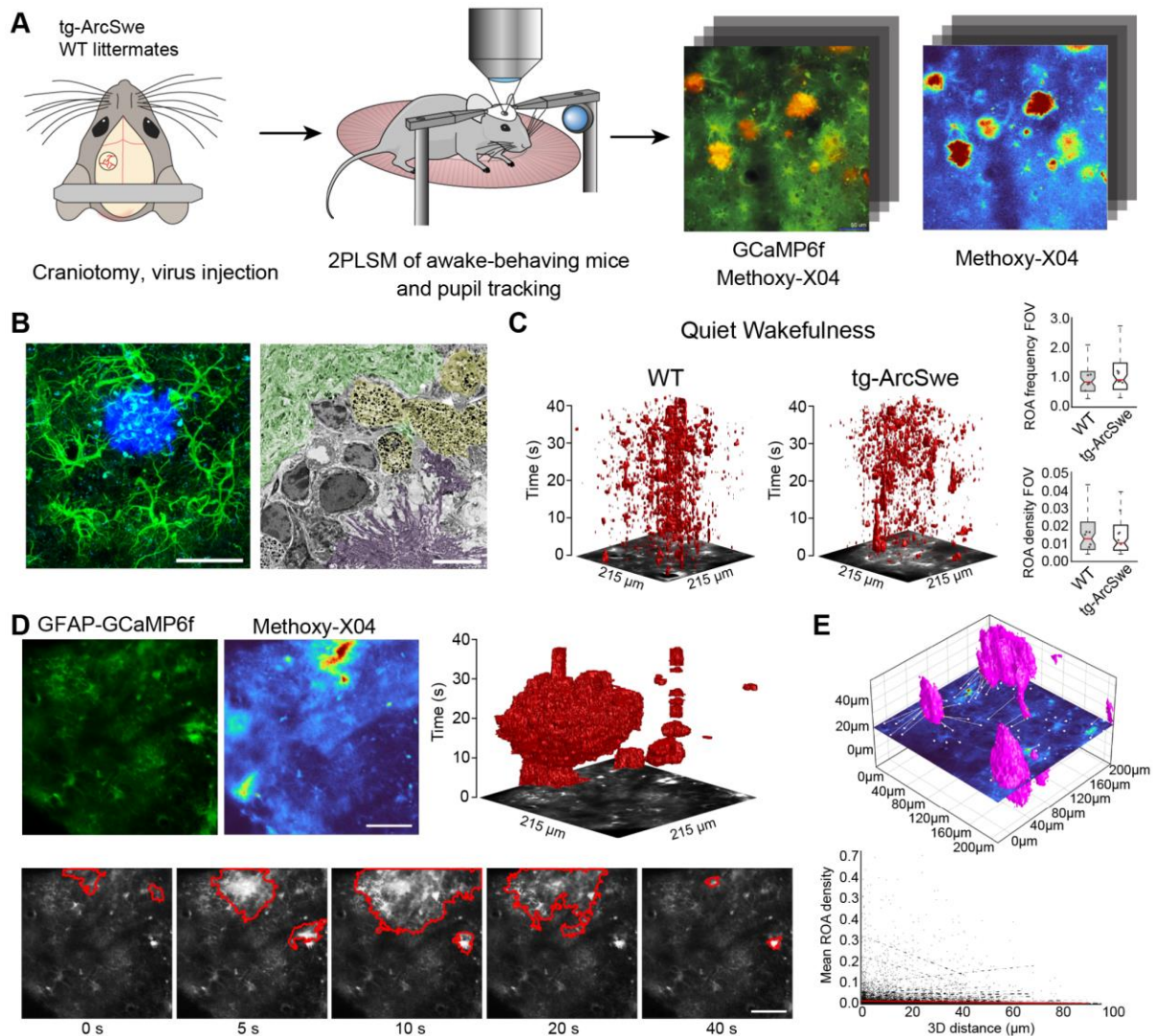
57

58 The field of astrocytic Ca^{2+} signalling is undergoing a revolution as developments in optical imaging
59 and genetically encoded fluorescent sensors now allow us to monitor these signals in awake-behaving
60 mice, without the confounding effects of anesthesia (Srinivasan et al. 2015; Bojarskaite et al. 2020).

61 Such studies have revealed exceedingly rich and complex astrocytic Ca^{2+} signalling ranging from
62 large activations of nearly all astrocytes in a field-of-view (FOV) under locomotion and startle
63 responses due to noradrenergic activity (Ding et al. 2013; Paukert et al. 2014), to small, localized
64 signals occurring spontaneously or as a response to local neuronal activity (Bindocci et al. 2017;
65 Stobart et al. 2018; Srinivasan et al. 2015). New analytical tools now also enable us to accurately
66 quantify and describe these signals (Y. Wang et al. 2019; Bjørnstad et al. 2021).

67

68 Here we show by two-photon microscopy that ~15 month old unanesthetized awake-behaving tg-
69 ArcSwe mice display attenuated behaviorally induced Ca^{2+} signalling in cortical astrocytes during
70 locomotion. These mice carry two mutations in the amyloid precursor protein gene, the Arctic
71 (E693G) and Swedish (KM670/6701NL) mutations, and exhibit amyloid- β deposits, a hallmark of
72 AD (Lord et al. 2006; Yang et al. 2011; Lillehaug et al. 2014; Philipson et al. 2009). As noradrenergic
73 signalling is known to be the most potent trigger of astrocytic Ca^{2+} signalling in startle responses and
74 locomotion, and pupil responses are regarded a faithful, although indirect, readout of noradrenergic
75 signalling in the brain during physiological conditions (Reimer et al. 2016; Zuend et al. 2020; Costa
76 and Rudebeck 2016), we compared the pupil responses to the astrocytic Ca^{2+} signals and found a
77 strong positive correlation in wild-type mice. No such correlation was present in the AD mice. This
78 points to a potential decoupling of neuromodulatory activation and astrocytic Ca^{2+} activity. Such
79 perturbed behaviorally induced astrocytic Ca^{2+} signalling may account for some of the cognitive
80 deficiencies observed in AD patients.



81

82

83 **Figure 1. Experimental setup and astrocytic Ca^{2+} signalling in behavioral quiescence.** (A) Virus encoding

84 GCaMP6f was injected into the somatosensory cortex of tg-ArcSwe mice and non-mutant littermates. After 3

85 weeks of recovery, mice were habituated to head-fixation on a disc-shaped treadmill, allowing the mice to move

86 freely at will. Methoxy-X04 was injected 24 hours prior to imaging to visualize amyloid plaques. During

87 imaging, both locomotor activity and pupil responses were recorded. (B) The mice were ~15 months of age

88 during experiments, at a time when they exhibited dense-core amyloid- β plaques. Left image: confocal

89 micrograph of an amyloid plaque (methoxy-X04, blue) and astrocytes (anti-GFAP, green). Scale bar: 40 μ m.

90 Right image: Electron micrograph showing a dense amyloid plaque (purple overlay), autophagic vacuoles

91 (yellow overlay) and relatively normal neuropil morphology (green overlay). Scale bar 2 μ m. (C) Astrocytic

92 Ca^{2+} signals during quiet wakefulness (absence of locomotion) in the form of regions-of-activity (ROAs)

93 displayed in an x - y - t 3D rendering where red regions denote signal. Box-and-whisker plots representing overall

94 Ca^{2+} signals in quiet wakefulness in tg-ArcSwe mice and littermates. (D) Example of pathological astrocytic

95 Ca^{2+} wave emanating from an amyloid plaque. Top left: average image projections of GCaMP6f fluorescence

96 and methoxy-X04, respectively. Top right: 3D x - y - t rendering of ROAs representing a pathological Ca^{2+} wave.

97 Bottom row: micrographs of the same pathological Ca^{2+} wave as in the 3D plot with the Ca^{2+} event outlined in

98 red. Scale bars: 50 μm . (E) 3D visualization of the imaging plane relative to amyloid plaques, with lines
99 representing shortest distance from plaque to ROI. We found a low correlation between distance to nearest
100 plaque and gross level of astrocytic Ca^{2+} signalling.

101 RESULTS

102

103 Two-photon imaging of awake-behaving tg-ArcSwe mice

104 To characterize astrocytic Ca^{2+} signalling in awake tg-ArcSwe mice and nontransgenic littermates we
105 employed two-photon microscopy of cortical layer 1–3 astrocytes in the somatosensory cortex
106 expressing GCaMP6f. The glial fibrillary acidic protein (GFAP) promoter was used to target
107 astrocytes (Fig 1A). Amyloid plaques were visualized *in vivo* by methoxy-X04 delivered by
108 intraperitoneal injection (Fig. 1A). Methoxy-X04 enters the brain and specifically stains parenchymal
109 $\text{A}\beta$ plaques and cerebrovascular deposits (Klunk et al. 2002), and has been used for *in vivo* imaging in
110 transgenic mice with amyloid plaques (Delekate et al. 2014; Kuchibhotla et al. 2009; Meyer-
111 Luehmann et al. 2008). Imaging was performed at ~ 30 Hz frame rate to capture fast populations of
112 astrocytic Ca^{2+} transients with simultaneous surveillance video recording of the mouse behavior,
113 movement of the treadmill as well as pupil dilations and constrictions to monitor the level of arousal
114 (Reimer et al. 2016). The mice were allowed to spontaneously move on a custom-built disc shaped
115 treadmill, and all mice exhibited both periods of quiet wakefulness (absence of locomotion), and
116 running (Supplementary Fig. 1). Astrocytic Ca^{2+} signals were analyzed using a newly developed
117 event-based Ca^{2+} signal analysis toolkit, outlining so-called regions-of-activity (ROAs), combined
118 with manually segmented regions-of-interests (ROIs) outlining astrocytic subcompartments
119 (Björnstad et al. 2021; Bojarskaite et al. 2020).

120 Astrocytes close to amyloid plaques express GCaMP6f

121 The tg-ArcSwe mice were imaged at ~15 months of age. At this age they present with amyloid- β
122 plaques throughout the cortical mantle, and score poorly on behavioral tasks (Codita et al. 2010;
123 Lillehaug et al. 2014; Lord et al. 2006)(Fig. 1B). A β -plaques were characterized by loss of cells and
124 severely perturbed tissue morphology, including autophagic vacuoles (Fig 1B). Even so, relatively
125 normal cellular morphology was present at short distances away from amyloid plaques, and astrocytes
126 faithfully expressed the GCaMP6f Ca²⁺ sensor 3 weeks after viral transduction (Fig. 1A,B).

127 Astrocytic Ca²⁺ signals in quiet wakefulness are preserved in tg-ArcSwe mice

128 In quiet wakefulness (defined as absence of locomotion), we found examples of long-lasting
129 pathological Ca²⁺ waves as reported previously in anesthetized mice (Delekate et al. 2014;
130 Kuchibhotla et al. 2009), often emanating in the vicinity of discernable amyloid plaques and
131 spreading to nearby astrocytes. Such Ca²⁺ waves were found in 10–15% of recordings from tg-
132 ArcSwe mice (Fig. 1D). The number of such clear pathological events were few compared to the
133 overall astrocytic Ca²⁺ signalling we found without the highly confounding effects of anesthesia.
134 Consequently, the gross level of astrocytic Ca²⁺ signalling was similar in mutant mice and their
135 littermates as measured by ROA frequency, ROA density (the active fraction of a compartment) as
136 well as event size and duration in the full field-of-view (FOV) and across the different astrocytic
137 subcompartments (Fig 1C and Supplementary Fig. 2). We were not able to detect a clear correlation in
138 astrocytic Ca²⁺ signalling measured by ROA density and the distance from nearest amyloid plaque (in
139 3D) (slope = -0.00020, Fig. 1E).

140

141 Uncoupling between pupil dilation and astrocytic Ca²⁺ responses during 142 spontaneous running in tg-ArcSwe mice

143 Locomotor behavior is known to be strongly correlated with astrocytic Ca²⁺ signalling (Paukert et al.
144 2014; Bojarskaite et al. 2020; Srinivasan et al. 2015), putatively through the activation of the
145 noradrenergic and cholinergic neuromodulatory systems in conjunction with local network activity
146 (Kjaerby et al. 2017). To investigate if the physiological astrocytic Ca²⁺ responses were preserved in
147 the tg-ArcSwe mice, they were allowed to move freely on a custom built disc-shaped treadmill
148 (Bojarskaite et al. 2020). All mice exhibited both running and behavioral quiescence, and the level of
149 running between the two genotypes were comparable (Supplementary Fig. 1). Running was
150 accompanied by an increase in pupil size and a brisk increase in astrocytic Ca²⁺ signalling typically
151 involving most of the astrocytes in the field-of-view (FOV) in both genotypes (Fig. 2A). When

152 astrocytic Ca^{2+} signals were analysed using a linear mixed effects regression model, a lower ROA
153 density rise rate was found in tg-ArcSwe mice when assessing the full FOV (0.31 in WT vs. 0.20 in
154 tg-ArcSwe, $p = 0.032$), and astrocytic processes (0.32 in WT vs. 0.20 in tg-ArcSwe, $p = 0.032$),
155 whereas the Ca^{2+} responses were not significantly different in astrocytic somata and endfeet (0.46 in
156 WT vs. 0.39 in tg-ArcSwe, $p = 0.23$, and 0.35 in WT vs. 0.30 in tg-ArcSwe, $p = 0.11$,
157 respectively)(Fig. 2B). Max ROA density values in WT vs. tg-ArcSwe were significantly different
158 when assessing the full FOV (0.63 vs. 0.42, $p = 0.033$), near significantly different when assessing
159 astrocytic processes and endfeet (0.72 vs. 0.53, $p = 0.053$ for processes and 0.69 vs. 0.51, $p = 0.068$
160 for endfeet), and not significantly different for astrocytic somata (0.81 vs. 0.71, $p = 0.25$)(Fig. 2B).
161 For mean ROA density values, see Supplementary Fig. 3.

162
163 Pupil responses are known to be a faithful indirect indicator of activity in the locus coeruleus in mice,
164 even though also the cholinergic neuromodulatory system plays a role for sustained pupil dilation
165 (Reimer et al. 2016). As norepinephrine is known to be a potent trigger of astrocytic Ca^{2+} signalling
166 (Bekar, He, and Nedergaard 2008; Srinivasan et al. 2015; Paukert et al. 2014), one would expect to
167 find a strong correlation between pupil dilations and astrocytic Ca^{2+} signals. This was indeed the case
168 for WT mice: When comparing ROA density rise rate and pupil dilation, we found a clear positive
169 slope in line with previous reports (Zuend et al. 2020). In transgenic mice, this correlation was lost, or
170 even reversed (Fig. C, slope of 0.80 in WT vs. -0.35 in tg-ArcSwe, $p = 0.007$), demonstrating an
171 uncoupling between pupil responses and astrocytic Ca^{2+} signalling in AD transgenic mice. Similarly,
172 when assessing max ROA density, we found a clear positive slope in WT, which was lost in tg-
173 ArcSwe (Fig. 2C, 2.06 in WT vs. -0.58 in tg-ArcSwe, $p = 0.00039$). Similar slopes were found when
174 comparing mean ROA density vs pupil dilation (Supplementary Fig. 3).

175

176

177

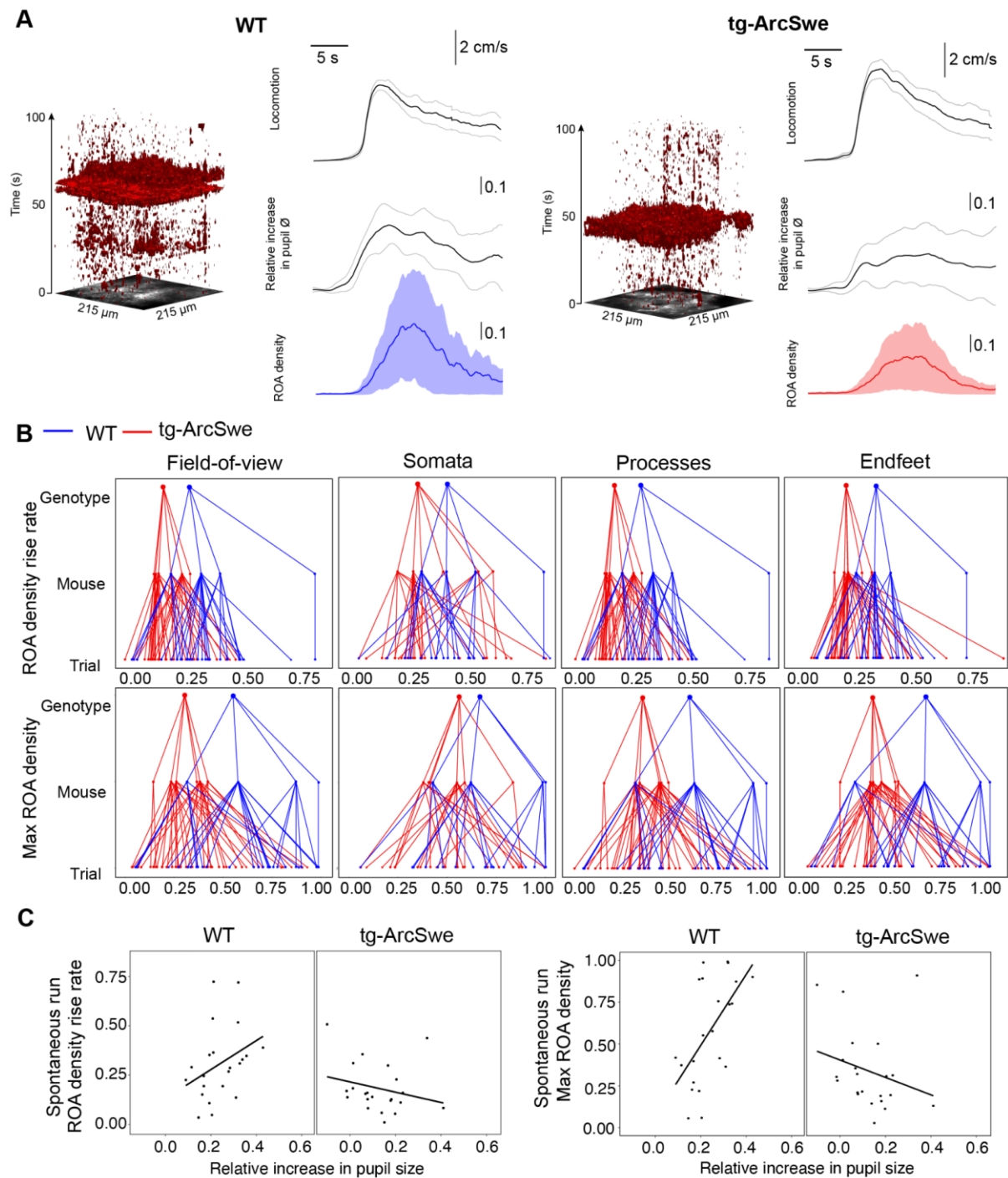
178

179

180

181

182



183

184 **Figure 2. Uncoupling of pupil dilation and astrocytic Ca^{2+} responses during spontaneous running.** (A)

185 Bouts of spontaneous running caused a pronounced increase in pupil size and an increase in astrocytic Ca^{2+}

186 signalling. ROAs presented as an $x-y-t$ 3D rendering where red regions denote signal. Locomotion trace show

187 mean response across trials with 95% confidence interval, pupil trace and ROA density traces show median

188 across trials \pm median absolute deviation. (B) Upper row: Plots showing the median level of ROA density rise

189 rate per genotype (red = tg-ArcSwe, blue = WT littermates), per mouse and per trial in the full FOV, astrocytic

190 somata, astrocytic processes and astrocytic endfeet. Lower row: Same as upper row, but showing median levels

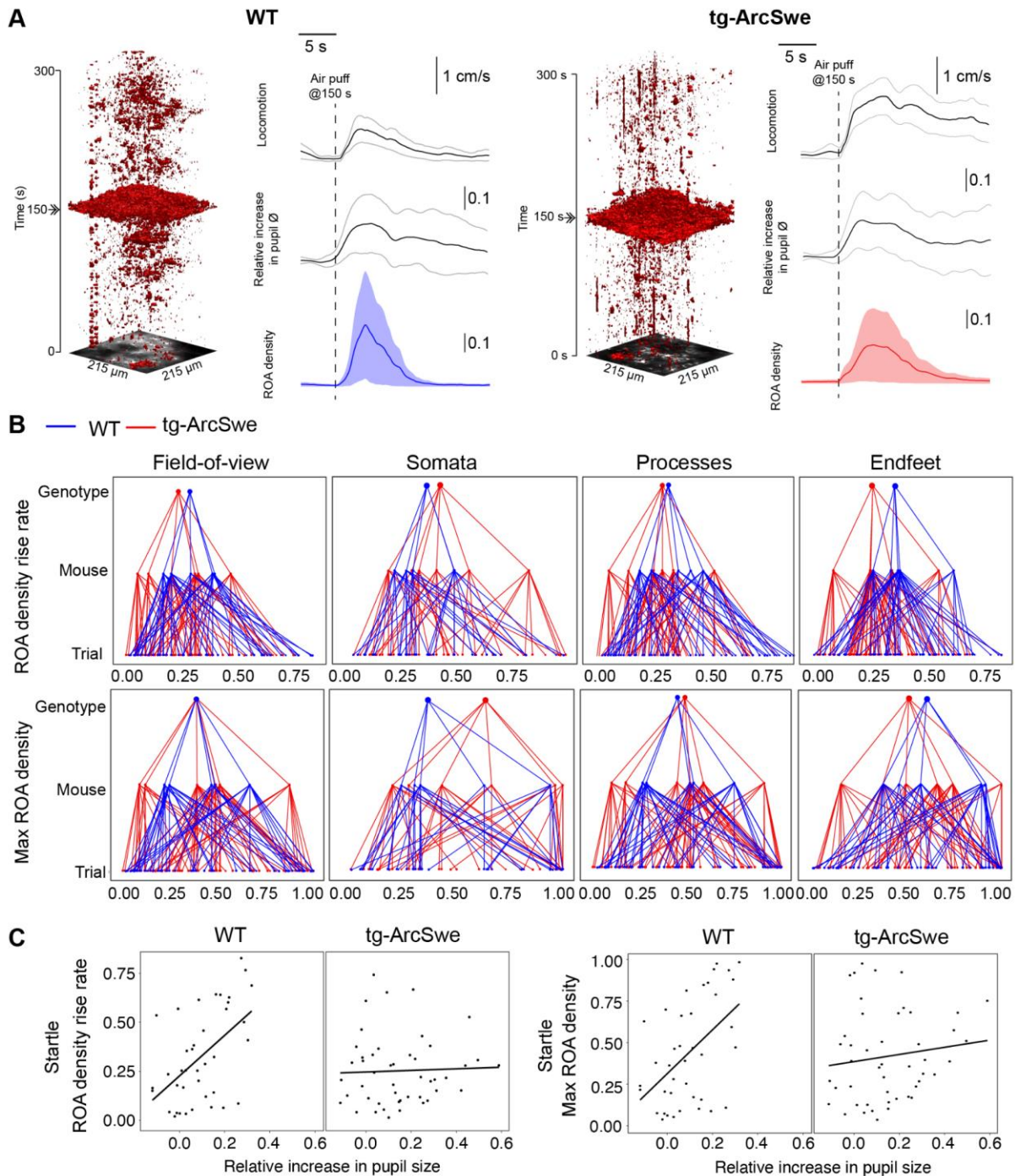
191 of max ROA density in the astrocytic subcompartments. (C) Scatterplots of ROA density rise rate and max ROA
192 density vs. relative increase in pupil size upon spontaneous running.

193 Uncoupling between pupil dilation and astrocytic Ca^{2+} responses during startle 194 in tg-ArcSwe mice

195 Another main trigger for astrocytic Ca^{2+} signals are startle responses that are mediated through an
196 activation of the noradrenergic system (Ding et al. 2013; Srinivasan et al. 2015). Even though
197 typically triggering running, the startle response could also trigger freezing behavior and is thought to
198 activate different subcortical networks than spontaneous locomotor behavior (Caggiano et al. 2018;
199 Ferreira-Pinto et al. 2018; Grillner and El Manira 2020). To characterize startle mediated astrocytic
200 activation in the two groups of mice, mice were subjected to 10 air puffs delivered at 10 Hz directed
201 to the vibrissa, nasal and facial region contralaterally to the recording side once per trial at 150 s in a
202 300 s two-photon imaging recording. Trials in which the mouse was spontaneously running at or
203 immediately before the air puff were excluded from the analyses. We found no signs of habituation to
204 the stimulus in terms of behavioral response (Supplementary Fig. 4). Interestingly, tg-ArcSwe mice
205 were more prone to react with running behavior during startle responses than WT littermates (Fig.
206 3A), consistent with previous reports of enhanced startle response in other mouse models of AD
207 (McCool et al. 2003). The level of pupil dilation was however similar in the two genotypes (0.17 vs.
208 0.12 relative increase in pupil size in WT vs. tg-ArcSwe, respectively, $p = 0.36$, 86 trials)(Fig. 3A).
209 When modelled with a mixed effects linear regression model, for ROA density rise rate, there was a
210 trend of lower Ca^{2+} responses in the full FOV, astrocytic processes and endfeet in tg-ArcSwe mice
211 (0.34 in WT vs. 0.23 in tg-ArcSwe, $p = 0.09$, 0.42 in WT vs. 0.31, $p = 0.09$ and 0.36 in WT vs. 0.25, p
212 $= 0.10$, respectively). No trend was evident in astrocytic somata (0.25 in WT vs. 0.23 in tg-ArcSwe, p
213 $= 0.8$)(Fig. 3B). Max ROA density was similar for the full FOV (0.36 in WT vs. 0.35 in tg-ArcSwe, p
214 $= 0.40$), astrocytic somata (0.37 in WT vs. 0.35 in tg-ArcSwe, $p = 0.83$), astrocytic processes (0.41 in
215 WT vs. 0.34 in tg-ArcSwe, $p = 0.39$), and astrocytic endfeet (0.41 in WT vs. 0.35 in tg-ArcSwe, $p =$
216 0.48). For mean ROA density values, see Supplementary Fig. 3.

217

218 However, the relationship between astrocytic Ca^{2+} responses and pupillary responses were highly
219 different in the two genotypes (Fig. 3D), with WT mice displaying a clear positive slope, while tg-
220 ArcSwe exhibited a slope close to zero (0.91 vs. -0.013 $p = 0.00043$ for ROA density rise rate, and
221 1.27 vs. 0.083 $p = 0.0043$ and max ROA density, respectively), suggesting an uncoupling between
222 pupillary responses and astrocytic Ca^{2+} responses in tg-ArcSwe mice similar to during spontaneous
223 running (Fig. 3C). Similar slopes were found when comparing mean ROA density vs pupil dilation
224 (Supplementary Fig. 3).



225

226 **Figure 3. Uncoupling of pupil dilation and astrocytic Ca^{2+} responses during startle.** (A) In an imaging trial
 227 of 300 s duration, mice were subjected to an air puff to the face/vibrissa contralateral to the imaging window at
 228 150 s. This caused an increase in locomotor activity, pupil dilation, and a pronounced increase in astrocytic Ca^{2+}
 229 signalling in both genotypes (right). Locomotion trace show mean response across trials with 95% confidence
 230 interval, pupil trace and ROA density traces show median across trials \pm median absolute deviation. Astrocytic
 231 Ca^{2+} signals in the form of ROAs displayed in an x - y - t 3D rendering where red denote signal (left). (B) Upper
 232 row: Plots showing the median level of the ROA density rise rate per genotype (red = tg-ArcSwe, blue = WT

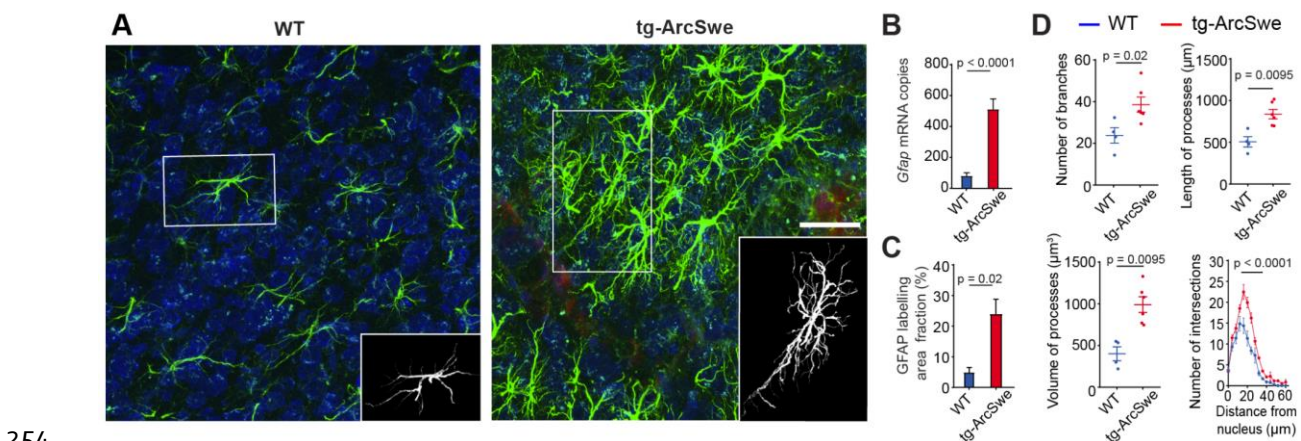
233 littermates), per mouse and per trial in the full FOV, astrocytic somata, astrocytic processes and astrocytic
234 endfeet. Lower row: Same as upper row but for max ROA density. (C) Scatterplots of ROA density rise rate and
235 max ROA density vs. relative increase in pupil size.

236 Widespread reactive astrogliosis in tg-ArcSwe mice

237 AD transgenic mouse models with high levels of beta-amyloid deposition exhibit reactive astrogliosis
238 (Rodríguez-Arellano et al. 2016), which might affect astrocytic Ca^{2+} activity (Shigetomi et al. 2019;
239 Sano et al., n.d.). We therefore assessed the level of reactive astrogliosis by assessing GFAP
240 expression by immunofluorescence, mRNA levels and morphometry of astrocytes in tg-ArcSwe mice
241 and WT littermates (Fig. 4).

242

243 We found a strong increase in levels of mRNA encoding GFAP (81.58 ± 19.56 for WT; $512.13 \pm$
244 66.95 for tg-ArcSwe, $p < 0.0001$, $n = 8$ animals in both groups) in tg-ArcSwe compared to WT
245 littermates (Fig. 4C). This was supported by a significantly higher GFAP labeling fraction in tg-
246 ArcSwe animals compared to WT littermates (Fig. 4B, $24.03\% \pm 4.80\%$ in tg-ArcSwe, $n = 6$ mice vs.
247 $4.77\% \pm 1.58\%$ in WT, $n = 4$ mice, $p = 0.02$). Morphometric analyses displayed a significantly higher
248 number of labelled astrocytic processes (38.63 ± 3.61 in tg-ArcSwe, $n = 6$ mice; 23.84 ± 3.72 in WT,
249 $n = 4$ mice; $p = 0.02$), as well as total length ($837.9 \mu\text{m} \pm 55.9 \mu\text{m}$ for tg-ArcSwe; $506.0 \mu\text{m} \pm 62.5$
250 μm for WT; $p = 0.0095$) and volume of processes ($990.9 \mu\text{m}^3 \pm 93.8 \mu\text{m}^3$ for tg-ArcSwe; $401.5 \mu\text{m}^3 \pm$
251 $82.9 \mu\text{m}^3$ for WT; $p = 0.0095$) in tg-ArcSwe mice compared to WT littermates (Fig. 4D). In addition,
252 astrocytes in the tg-ArcSwe mice exhibited significantly more branching points at the distance 16–32
253 μm from the nucleus ($p < 0.0001$).



254
255 **Figure 4. Widespread reactive astrogliosis in tg-ArcSwe mice.** (A) Representative micrographs labelled with
256 anti-GFAP antibodies (green) and anti-NeuN antibodies (blue). Scale bar: 40 μm . (B) *Gfap* mRNA expression
257 was considerably higher in tg-ArcSwe mice ($p < 0.0001$, $n = 8$ animals in both groups). (C) The area fraction of
258 GFAP labelling was significantly higher in tg-ArcSwe mice compared to controls ($n = 6$ tg-ArcSwe and 4 WT
259 littermates). (D) Astrocytes were isolated (inset in A) and analyzed with Simple Neurite Tracer (SNT) plugin in
260 FIJI ImageJ. Tg-ArcSwe mice displayed an increase in the total number of branches ($p = 0.02$), the length and

261 volume of processes ($p = 0.0095$ and $p = 0.095$, respectively) of the GFAP labelled astrocytes ($n = 8$ astrocytes
262 from each animal. 6 tg-ArcSwe and 4 WT littermates), as well as an increased number of branching points and
263 intersections at 16–32 μm distance from the nucleus ($p < 0.0001$).

264 Discussion

265 Astrocytic Ca^{2+} signalling is emerging as a key component of signal processing in the brain and
266 figures prominently in brain state transitions and memory formation (Poskanzer and Yuste 2016,
267 2011; Adamsky et al. 2018; Bojarskaite et al. 2020; Vaidyanathan et al. 2021). Aberrant astrocytic
268 Ca^{2+} signalling could hence be implicated in the perturbed cognition seen in dementia. Indeed,
269 previous studies have shown increased astrocytic Ca^{2+} signalling and spreading pathological Ca^{2+}
270 waves in AD mouse models (Kuchibhotla et al. 2009; Delekate et al. 2014). Based on these studies in
271 anesthetized animals and other studies (Haughey and Mattson 2003; Lim et al. 2013; Abramov,
272 Canevari, and Duchen 2004, 2003; Verkhratsky 2019) the current concept is that aberrant signalling
273 to some degree is spatially coupled to amyloid deposits – the pathological hallmark of Alzheimer's
274 disease.

275 Methodological advances now allow astrocytic Ca^{2+} signals to be studied in awake animals.
276 Benefitting from this opportunity we show that tg-ArcSwe mice sustain a pattern of behaviorally
277 induced astrocytic Ca^{2+} signalling similar to that found in littermate controls. However, the signals are
278 weaker than in controls and do not display the correlation with pupil responses typically seen in wild
279 type animals. The behaviorally induced Ca^{2+} signals bear no clear spatial correlation to amyloid
280 plaques. We conclude that elimination of anaesthesia unveils a new dimension of Ca^{2+} signalling,
281 superimposed on the locally induced signals described in previous studies. The uniform attenuation of
282 the behaviorally induced signals in tg-Arc-Swe mice and their uncoupling from pupil responses point
283 to a potential perturbation of neuromodulatory control.

284 Astrocytic Ca^{2+} signalling in awake behaving mice is dominated by norepinephrine-induced astrocytic
285 Ca^{2+} signals across the cortical mantle in relation to locomotor or startle responses (Srinivasan et al.
286 2015; Ding et al. 2013). The downstream effects of these synchronized, global Ca^{2+} signals coupled to
287 arousal are not fully understood, but they may play a role in altering the levels of extracellular K^+ (F.
288 Wang et al. 2012), release of gliotransmitters such as glutamate or ATP (Kjaerby et al. 2017; Haydon
289 and Nedergaard 2014) or metabolic supply (Zuend et al. 2020). Independent of what are the exact
290 downstream mechanisms, there are reasons to believe that astrocytes serve as actuators of the
291 noradrenergic neuromodulatory system, presumably exerting noradrenergic effects on neural network
292 processing and ultimately affecting cognitive function (Ye et al. 2020; Holland, Robbins, and Rowe
293 2021; Poskanzer and Yuste 2016).

294 The cause of perturbed astrocytic Ca^{2+} responses during locomotion responses in AD mice in our
295 experiments is not entirely clear. Firstly, we find prominent reactive astrogliosis throughout the brains
296 of the mice we studied. Although still sparsely investigated, both attenuated and increased Ca^{2+}
297 signalling have been demonstrated in various models of reactive astrogliosis, but so far without a clear
298 understanding of the mechanisms involved (Shigetomi et al. 2019). Widespread reactive astrogliosis
299 is nonetheless highly likely to perturb the physiological signalling of astrocytes, as prominent changes
300 in the expression of key receptors and molecules of intracellular pathways are known to occur (Habib
301 et al. 2020; Escartin et al. 2021). Secondly, the primary norepinephrine nucleus in the brain, locus
302 coeruleus, is known to be affected early in AD, both in humans and in animal models (Weinshenker
303 2018; Jacobs et al. 2021; Braak and Del Tredici 2011), and perturbed noradrenergic function is likely
304 an important factor both in disease progression in AD patients and accounting for the cognitive
305 decline of AD patients (Weinshenker 2018; Peterson and Li 2018; Holland, Robbins, and Rowe
306 2021). Restoring noradrenergic signalling in AD mice with perturbed noradrenergic signalling
307 pharmacologically or by pharmacogenetics have been demonstrated to be beneficial (Holland,
308 Robbins, and Rowe 2021). In our study we find a largely retained level of pupil response in the AD
309 mice during startle responses, which under physiological circumstances would suggest that the
310 noradrenergic system was working normally, as a strong correlation between locus coeruleus activity
311 and pupil responses have been established (Reimer et al. 2016; Costa and Rudebeck 2016). The
312 underlying connectivity that enables the pupils to be faithful readouts of the noradrenergic system is
313 to the best of our knowledge not fully established, even though spinal projections from locus
314 coeruleus have been demonstrated (Hancock and Fougousse 1976; Costa and Rudebeck 2016;
315 Liu et al. 2017). Our finding of a decoupling between astrocytic Ca^{2+} signalling and arousal-induced
316 pupillary dilation, could be due to perturbed connectivity between locus coeruleus and the relevant
317 nuclei or projections controlling activity in the superior cervical ganglion and consequently the
318 sympathetic projections to the pupils. Lastly, our observations could be explained by a combination of
319 these factors, namely altered intrinsic astrocytic responses in reactive astrogliosis combined with
320 perturbations in the correlation between locus coeruleus and pupillary responses. Future studies are
321 warranted to pinpoint the molecular mechanisms at play.

322 Previous studies have shown mixed results regarding an effect of plaque-astrocyte distance, with
323 reports of both hyperactivity close to plaques (Delekate et al. 2014) and no such correlation except for
324 plaques serving as initiation sites for pathological intercellular Ca^{2+} waves (Kuchibhotla et al. 2009).
325 In our awake-behaving mice, we found no clear correlation between Ca^{2+} activity and 3D distance
326 reconstruction of plaque positions relative to the imaging plane (Fig. 1E). The apparent discrepancies
327 in the literature and the present study may be due to different AD mouse models, different age groups
328 investigated, different Ca^{2+} indicators employed or lastly the effects of removing anesthesia allowing

329 for a much richer repertoire of astrocytic Ca^{2+} signalling to emerge, effectively masking a potential
330 weak correlation.

331

332 Astrocytes have a highly complex and specialized morphology, and this morphology is known to
333 change in reactive astrogliosis (Escartin et al. 2021). The majority of astrocytic processes are much
334 smaller than what can be clearly delineated by non-super resolution optical microscopy, but to what
335 extent these small processes are altered in reactive astrogliosis is unknown, although the astrocytic
336 territories are known to be preserved (Wilhelmsson et al. 2006). We cannot rule out that gliosis-
337 induced morphological changes in combination with potential subtle differences in GCaMP6f
338 expression and elevated baseline intracellular Ca^{2+} concentration (Kuchibhotla et al. 2009) may
339 influence our results. However, the ability for the whole FOV to be activated during spontaneous
340 running and startle responses and the lack of correlation (if anything a negative correlation) between
341 distance to the nearest amyloid plaque and gross level of Ca^{2+} signaling suggests that our findings are
342 not due to degree or pattern of sensor expression.

343

344 The present study underscores the importance of studying astrocytic Ca^{2+} signals in unanesthetized
345 mice, and to carefully consider animal behavior when interpreting astrocytic Ca^{2+} dynamics. By lifting
346 the confounding effects of anesthesia we found that the astrocytic hyperactivity previously reported in
347 Alzheimer's disease mouse models was only a part of the total picture. At first glance, the
348 physiological Ca^{2+} responses were remarkably well preserved, and not characterized by a general
349 increase in astrocytic Ca^{2+} signalling. However, behavior like quiet wakefulness and locomotion are
350 not static entities, and the degree of activation of all relevant parameters needs to be taken into
351 account with statistical modelling to be able to conclude if there are relevant differences between the
352 genotypes. We were able to demonstrate attenuated Ca^{2+} dynamics and an uncoupling between
353 astrocytic Ca^{2+} signalling and arousal in the tg-ArcSwe mice, and given the growing spectrum of roles
354 ascribed to astrocytic Ca^{2+} signalling in higher brain functions, the present findings may highlight one
355 cause for the cognitive decline of AD patients.

356

357

358 MATERIALS AND METHODS

359 Animals

360 Tg-ArcSwe mice carry a human A β PP cDNA with the Arctic (p. E693G) and Swedish (p.
361 KM670/671NL) mutations where the human A β PP gene is inherited only from male mice to ensure a
362 more uniform onset of A β -deposition (Lillehaug et al. 2014). The transgenic animals develop

363 parenchymal A β -plaques from 6 months of age, and cerebral amyloid angiopathy (CAA) from 8
364 months of age (Yang et al. 2011; Lord et al. 2006). 6 tg-ArcSwe mice and 5 WT littermates (both
365 males and females) were used in this study. Sample sizes were determined based on our previous
366 studies using similar techniques (no power calculations were performed). No randomization or
367 blinding was performed. Genotyping was performed as previously described with primers annealing
368 to the Thy1-promoter and the human APP-transgene (Lord et al 2006). The animals were housed
369 under standard conditions at a professional veterinarian facility with 12-hour dark-light cycles and
370 unrestricted access to food and water. All animal procedures were in accordance with the National
371 Institutes of Health Guide for the care and use of laboratory animals and approved by the Norwegian
372 Food Safety Authority (project number: FOTS #11983).

373 Viral transduction and delivery of fluorophores

374 Serotype 2/1 recombinant adeno-associated virus (rAAV) from plasmid construct pAAV-GFAP-
375 GCaMP6f (Chen et al. 2013) was generated (rAAV titers about $1.0\text{--}6.0 \times 10^{12}$ viral genomes/mL) and
376 used for visualizing astrocytic Ca²⁺ signalling. GCaMP6f was amplified by PCR from pGP-CMV-
377 GCaMP6f with 5' *Bam*HI and 3' *Hind*III, and sub-cloned into the recombinant rAAV vector pAAV-
378 6P-SEWB (Shevtsova et al. 2005) for generating pAAV-SYN-GCaMP6f. The human glial fibrillary
379 acidic protein (*GFAP*) promoter (Hirrlinger et al. 2009) was inserted with *Mlu*I and *Bam*HI into
380 pAAV-SYN-GCaMP6f construct for obtaining pAAV-*GFAP*-GCaMP6f. Serotype 2/1 rAAVs from
381 pAAV-*GFAP*-GCaMP6f was produced (Tang et al. 2015), and purified by AVB Sepharose affinity
382 chromatography (Smith, Levy, and Kotin 2009), following titration with real-time PCR (rAAV titers
383 about $1.0\text{--}6.0 \times 10^{12}$ viral genomes/mL, TaqMan Assay, Applied Biosystems). To visualize amyloid
384 plaques, 7 mg/g methoxy-X04 (Syverstad Skaaraas et al. 2021) dissolved in 0.1 M phosphate buffer
385 saline (PBS), was injected intraperitoneally 24 hours prior to imaging. We found that one injection
386 provided enough signal to outline amyloid plaques for up to three days.

387

388 Surgical preparation

389 Mice were anaesthetized with isoflurane (3% for initiation, then 1–1.5% for maintenance) in room air
390 enriched with 20% pure oxygen, and given buprenorphine 0.1 mg/kg s.c. preemptively for analgesia.
391 Bupivacain was administered subcutaneously over the skull, and left for 10 minutes before a boat
392 shaped skin flap was removed. After removing the skin, a 2.5 mm diameter craniotomy was drilled
393 over the somatosensory cortex with center coordinates 3.5 mm lateral and -1.5 mm posterior to
394 Bregma. Virus was injected (70 nL at 35 nL/min at 200 μ m depth from the brain's surface) at three
395 evenly spaced locations positioned to stay clear of large blood vessels, and a glass plug consisting of
396 two coverslips glued together were placed in the craniotomy, slightly pressing the dura to prevent

397 dural overgrowth (Bojarskaite et al. 2020). The surrounding area of the skull was sealed with
398 cyanoacrylate glue and a layer of dental cement. Post-operatively the mice were given meloxicam 2
399 mg/kg for two days. Only animals with normal post-operative recovery were included in the study.
400 Mice were left to recover for a minimum of two weeks before habituation to head-fixation and
401 imaging.

402

403 Two-photon microscopy

404 After recovery, the animals were imaged in layers 1–3 of the barrel cortex using a two-photon
405 microscope (Ultima IV from Bruker/Prairie Technologies, Nikon 16X, 0.8 NA water-immersion
406 objective model CFI75 LWD 16XW, Spectra-Physics InSight DeepSee laser, Peltier cooled
407 photomultiplier tubes model 7422PA-40 by Hamamatsu Photonics K.K.). An excitation wavelength
408 of 990 nm was used for GCaMP6f imaging, and separate recordings were made using 790 nm
409 excitation light for imaging methoxy-X04, and 890 nm for Texas-Red labelled dextran for
410 visualization of the vasculature. Image time series were recorded at 30Hz. 3D volume recordings of
411 the morphology and plaque locations were performed in a subset of experiments. All images were
412 recorded at 512x512 pixels with a resolution of approximately either 0.42 or 0.67 μm per pixel (FOV
413 of 215x215 μm , or 343x343 μm , respectively). For imaging, the mice were head-fixed to a custom
414 build stage that allowed free locomotion on a wheel attached to a rotary encoder. During experiments
415 the mice were monitored with an IR sensitive camera, illuminated by an IR LED diode. A second
416 camera was used to capture the pupil dynamics (see below). Air-puffs to elicit startle responses were
417 delivered by a Picospritzer III (Parker). Instrument synchronization and data acquisition were
418 performed with a custom-made LabVIEW 2015 (National Instruments) virtual instrument.

419 Behavioural analysis

420 Mouse locomotion was recorded with a rotary encoder connected to the running wheel. Locomotion
421 signal was captured using a National Instruments data acquisition card using a counter task in the NI
422 Max software, activated through a custom LabView (2015) VI. Data was processed with custom
423 MATLAB scripts to classify running and quiet wakefulness. Criteria for run and quiet wakefulness
424 episodes were validated by manual observation, and defined as follows: Running was defined as
425 continuous segment of at least 4 s forward wheel motion at over 30 degrees/s, no movement faster
426 than 20 degrees/s the last 10 seconds prior to start of running. Spontaneous running was not defined
427 within 30 seconds following air-puff. Quiet wakefulness was defined as continuous segment of at
428 least 10 s duration with less than 2 degrees/second locomotion, as well as no locomotor activity faster
429 than 2 degrees/s for 15 seconds before segment start. Quiet wakefulness episodes were not defined

430 within 30 seconds following air-puff. Quiet wakefulness periods were reviewed manually through the
431 IR-surveillance video recordings to ensure animals were awake when sitting still.

432 Pupillometry

433 Pupil size was recorded with a Basler Dart USB camera (daA1600-60um) with a 25mm fixed focal
434 length lens and 2X fixed focal length lens extender (Edmund optics, items #59-871 and #54-356).
435 The pupil was back-illuminated with the spillover light from the two-photon microscope laser coming
436 through the cranial window (Yüzgeç et al. 2018). As two-photon imaging must be conducted in the
437 dark where the pupil would be fully dilated, we illuminated the mouse eye contralateral to the
438 recording side using 470 nm blue light fiber, with a shielding to avoid light contamination, to slightly
439 constrict the pupil. Pupil size was manually delineated for time periods of isolated runs and startle
440 using a custom build tool developed in MATLAB 2020a. The ratio of pupil to eye-size ratio was
441 calculated and used in the analysis.

442 Image processing and analysis

443 Recordings were exclusively processed using MATLAB 2018a to 2020b. We used our recently
444 published imaging analysis toolbox ‘Begonia’ to remove motion artefacts, mark ROIs and perform
445 event-based Ca^{2+} signal detection (regions-of-activity method; ROA). Methods and algorithms related
446 to this processing pipeline are described in detail in Bjørnstad et al. 2021 (Bjørnstad et al. 2021).
447 Astrocytic Ca^{2+} signals were detected using the ROA method, and the ROA density (i.e. fraction of
448 the compartment analyzed being active) and ROA frequency in the whole FOV or in anatomical
449 subcompartments were calculated.

450

451 3D amyloid plaque mapping

452 Before any recording, z-stacks of images at 5 μm intervals taken at 512 x 512 pixels were recorded
453 while illuminating the tissue with 790 nm laser light. The stacks started approximately at or below
454 dura mater and extended 100–200 μm down. All other recordings were undertaken inside this mapped
455 volume to ensure plaques outside the imaging plane were accounted for. For each imaged time series
456 inside the volume we recorded an additional single image at 790 nm to ensure the precise location of
457 plaques were known. Plaque locations were detected by binarizing the stack at a manually set
458 threshold at which the morphology of plaques were visible. The binarized single images were used to
459 manually align the 2D time series data with the 3D plaque volume. The resulting 3D binary image had
460 small points removed using the Matlab function bwareaopen.

461

462 Tissue processing

463 All animals were sacrificed after final imaging procedures, at the age of 18 months. The animals were
464 anesthetized with Isofluran Baxter (IsoFlo, Abbot Laboratories) and intraperitoneally injected with
465 ZRF mixture (Zolazepam 3.8 mg/ml, Tiletamin 3.8 mg/ml Xylazine 0.45 mg/ml and Fentanyl 2.6
466 µg/ml) before transcardial perfusion with 4°C 2% dextran in 0.1 M phosphate buffer (PB) for
467 approximately 30 seconds, immediately followed by 4% formaldehyde (FA) in PB for 10 minutes at
468 the speed of 6 ml/min. Following perfusion, the brains were extracted and post fixed by immersion in
469 the fixative at 4°C overnight protected from light. The tissue was stored in 0.1 % FA in PB at 4°C
470 protected from light until further processing. Cryoprotective steps in graded sucrose solution (10%,
471 20%, and 30% sucrose in PB) were performed before the brains were cut on a freeze microtome
472 (Thermo Scientific™ Microm KS 34) in 40 µm free floating coronary sections and stored in 0.1 %
473 FA in PB at 4°C protected from light until usage. In addition, 8 tg-ArcSwe animals and 8 wild type
474 littermates were sacrificed at 12 months of age and used for qPCR analysis. These animals were
475 anesthetized as described above and decapitated. The brains were extracted, and the left hemisphere
476 was dissected into the frontal cortex, hippocampus, cerebellum and the rest of the brain. This tissue
477 was frozen and stored in -80°C pending analysis.

478 RNA isolation and real time PCR

479 48 hours prior to RNA extraction, the samples were suspended in RNAlater™-ICE (Ambion; Cat#:
480 AM7030). To isolate total RNA from the frontal cortex tissue samples, the RNeasy Mini Kit
481 (QIAGEN, Hilden, Germany), including the on column DNase digestion, was used. The RNA
482 concentration and integrity were determined using a NanoDrop 2000c spectrophotometer
483 (ThermoFisher Scientific) and ethidium bromide visualization after agarose gel electrophoresis,
484 respectively. Following the manufacturer's protocol, 1 µg of total RNA was reverse - transcribed into
485 cDNA with Oligo (dT)₁₅ using the GoScript Reverse Transcription System (Promega, Madison, USA,
486 Cat#: A5001). All the cDNA samples were diluted in Tris-EDTA buffer (pH 8.0) to a final
487 concentration of 2.5 ng/µl. Real-Time PCR was carried out in a total volume of 20 µl, containing 2x
488 AB Power SYBR® Green PCR Master Mix (ThermoFisher Scientific) with gene specific primers (at
489 a final concentration of 200 nM) and 2 µl cDNA samples. Amplification was performed on the
490 StepOnePlus system (Applied Biosystems) with the following conditions: 95°C for 10 minutes,
491 followed by 40 cycles of 95°C for 15 seconds and 60°C for 1 minute, followed by melting curve
492 analysis to check for unspecific products. Each sample was run in duplicates. Using the NormFinder
493 software (Andersen et. al. 2004), *HPRT1* was determined as an internal control for normalization of
494 the gene expression. The primers were designed online using Primer-BLAST and setting the amplicon
495 size to a maximum of 200 bp. The primers designed span exon-exon junction, and standards prepared

496 as previously described (Rao et al. 2021). Details of the *Gfap* forward and reverse primer are
497 presented in Table 1.

Gene	Protein names	Accession	Forward (5')	Reverse (3')
<i>Gfap</i>	Glial fibrillary acidic protein	NM_010277.3	GCACTCAATACGAGGCAGT G	GCTCTAGGGACTCGTTCGT G

498 Table 1. Primer used for mRNA quantification.

499 Immunohistochemistry

500 One section from each animal was chosen for quantification of astrogliosis and washed in PBS 0.01
501 M for 10 minutes, followed by two times in 0.1% TritonX100 in PBS (PBST) for 5 minutes. The
502 PBST was removed and blocking (10% normal donkey serum (NDS), 1 % bovine serum albumin
503 (BSA), 0.5% Triton X100 in PBS) performed for one hour at room temperature. This was directly
504 followed by incubation overnight at room temperature with primary antibodies (GFAP; host: mouse;
505 diluted 1:1000; Sigma-Aldrich; Cat# MAB360. GFP; host: chicken; diluted 1:2000; Abcam; cat#
506 ab13970) diluted in antibody solution (ABS; 3% NDS, 1 % BSA, 0.1 % Triton X100 in PBS). The
507 following day the sections were rinsed in 0.1% PBST two times for 1 minute, followed by three times
508 for 10 minutes. Secondary antibodies (CY5 Donkey Anti-Mouse; Jackson ImmunoResearch Labs;
509 Cat# 715-175-151. CY3 Donkey Anti-Chicken; Jackson ImmunoResearch Labs; Cat#703-165-155)
510 were spun in a centrifuge for 10 minutes at 13000 rpm, diluted 1:500 in ABS, and the sections
511 incubated for 1 hour at room temperature. After the second incubation, the sections were washed in
512 PBS for 10 minutes, three times. Propidium iodide (diluted 1:5000 in 0.01 M PBS; Sigma Aldrich;
513 Cat # 04511 (Cellstain double staining kit)) for nuclear staining was added for 10 minutes, before
514 rinsing the sections twice for 5 minutes in PBS. All sections were transferred to distilled water and
515 mounted with ProLong Gold antifade reagent (ThermoFisher Scientific; Cat# P36934). They were
516 stored in -20 °C protected from light until confocal imaging. For electron microscopy: EM standard
517 procedure was followed for embedding and preparing of the tissue (Yang et al. 2011). For enhancing
518 the contrast, uranyl acetate (Fluorochem) in double distilled water and lead citrate was used. The
519 sections were examined in a transmission electron microscope (TECNAI 12).

520

521 Confocal imaging

522 GFP-positive astrocytes (indicating GCaMP6f expression) were used to locate the appropriate cortical
523 area used for in vivo imaging. Only sections where we could locate positive GFP staining within the
524 cortex corresponding to the image area were chosen for confocal imaging and further analysis. All
525 single plain and z-stack images were acquired using a Zeiss LSM 710 confocal microscope. To
526 provide overview and verify that the correct area was identified, one tile scan of 3072 x 3072 pixels
527 was achieved with a 40x objective (1.20; water korr M27) using 3 channels (CY2, CY3 and CY5) for
528 wild types and 4 channels (Dapi, CY2, CY3 and CY5) for tg-ArcSwe. Next, one z-stack of 2048 x
529 2048 pixels (40x objective; 1.20; water korr M27) from within the GFP positive area was acquired
530 from cortical layer 2. All single plane and z-stack images were obtained with identical settings. In
531 addition, a z-stack of 1024 x 1024 pixels was obtained (40x objective; 1.20; water korr M27) outside
532 the located GFP positive stained area. No post-processing on the analysed images were performed.

533 3D reconstruction analysis of astrocytes

534 This procedure was adapted from the details outlined in Tavares et al. (Tavares et al. 2017) that utilize
535 the free software plugin Simple Neurite Tracer (SNT) of FIJI-ImageJ (Longair, Baker, and Armstrong
536 2011). Only astrocytes with a single nucleus where at least $\frac{2}{3}$ of the circumference was covered by
537 GFAP staining were selected for 3D reconstruction. Astrocytes with processes touching the borders of
538 field of view were omitted. 8 randomly selected astrocytes from each z-stack (2 from each image
539 quadrant) obtained within the GFP positive imaging area were used for analysis. To quantify and
540 visualize the morphological complexity of the astrocytes, we analysed the number of processes, total
541 length of processes in μm , process thickness (μm^3) and number of intersections (provided from the
542 Sholl analysis).

543 GFAP area fraction analyses

544 Z-projections based on the CY5-channel to visualize GFAP positive astrocytes of all stack images
545 were rendered using the FIJI-ImageJ software (Schindelin et al. 2012). The images were blinded to
546 the analyst, converted to 8 bit images and the scale removed. The threshold was manually adjusted so
547 that only what was considered to be GFAP positive staining was red, and a percentage value of
548 positive staining in the image was obtained.

549 Statistical analysis

550 Astrocytic Ca^{2+} signals were studied by means of the ROA density – a number between 0 and 1
551 indicating the fraction of the compartment with activity. Here, the area may be the entire field-of-view
552 (FOV), or we may limit ourselves to the area identified as belonging to cellular subcompartments; the

553 astrocytic processes, somata or endfeet. In each trial we had time series of ROA density lasting
554 around 300 s (approximately 9000 frames). Within each trial, the startle period was defined as starting
555 from the air puff at 150 s and lasting 600 frames (~20 seconds). In addition, one or more time periods
556 within the trial could be identified as spontaneous runs, or as periods of quiet wakefulness. A first
557 important question concerns the choice of summary statistics adequately describing the Ca^{2+} response
558 in such periods of interest (runs and startle), which are dynamic behavioral states that entail both
559 acceleration, steady locomotion and deceleration. We have studied the mean and max ROA density
560 and the ROA density rise rate which is defined as the *maximal increase in ROA density over a*
561 *maximum of 50 frames*. Initial explorations indicated that the main results are fairly robust to the
562 choice of window length, and 50 frames appeared to be a sensible choice compared to the kinetics of
563 astrocytic Ca^{2+} signals. The ROA density rise rate is meant to capture some of the dynamics in
564 astrocytic Ca^{2+} signaling, and can be understood as the maximum acceleration inside the time period
565 of interest. The rise rate has a high correlation with the maximum, and if the length of the window is
566 increased sufficiently these two statistics tend to become almost identical (since most traces are close
567 to zero at some point in the trial). See the Supplementary Fig. 5A which displays both the max ROA
568 density and the rise rate in an example.

569
570 Pupil size measurements had a coarser time resolution than for the astrocytic Ca^{2+} signals; see
571 example in Supplementary Fig. 5B, showing the pupil sizes around a startle response. The pattern in
572 the figure – a sharp increase in pupil size after air puff, before a gradual decline – was quite typical.
573 Therefore, we chose to only consider the measurements in a time-window of 6.67 seconds on each
574 side of the airpuff (or start of running). We defined the *pupil dilation* as the relative increase in the
575 ratio of pupil diameter to eye diameter, inside this window. In other words, we calculate the average
576 ratio before the air puff (or start of running) and after the airpuff, compute the difference and divide
577 by the average before the air puff.

578 Interpreting hierarchical plots

579 We have chosen to present some of our data in the form of *hierarchical plots* (see Figure 2B and C,
580 Figure 3B and C, and Supplementary Fig. 1, 2 and 3). These plots allow the reader to assess the
581 degree of separation between the genotypes and at the same time get an impression of the *variation at*
582 *different levels of the analysis* – in our case, the variation between different mice of the same
583 genotype and the variation between repeated measurements on the same mouse. At the lowest level –
584 the trial level – we have points representing the observations themselves. For the spontaneous runs,
585 there are sometimes more than one run per trial and in that case the points are the median ROA
586 density rise rate in these runs. The maximal number of spontaneous runs in a single trial was 5
587 (average: 1.6 runs per trial). At the middle level we have the median ROA density rise rate for each

588 mouse, and at the top level the median ROA density rise rate for each genotype. The lines between the
589 levels indicate which observations belong to each mouse, and to each genotype respectively. We have
590 made similar plots for the max ROA density also. The hierarchical plots are a useful tool for
591 exploratory analysis. They are also meant to promote transparency in scientific reporting, and to
592 highlight the importance of intra-group variation. Still, it is important to realize that the impression
593 conveyed by the plots might not be identical to the results from statistical modelling. In the plots, we
594 do not include the influence of various technical and biological covariates which one typically would
595 include in a statistical model. Some of the variation between observations belonging to the same
596 mouse and between different mice of the same genotype may be explained by such covariates, as we
597 will see in the next section.

598 Modelling

599 Statistical analyses were conducted in R (version 4.1.1). The ROA density rise rate was modelled by
600 linear mixed effect regression models which were fitted using the glmmTMB package (Brooks,
601 Kristensen, and Van Benthem 2017). We conducted two sets of analyses: (i) to investigate potential
602 differences in ROA density rise rate between the two genotypes; (ii) to investigate the relationship
603 between ROA density rise rate and the pupil dilation, including potential differences between the two
604 genotypes with respect to this relationship. For (i) the coefficient of primary interest is the one
605 belonging to the genotype variable, while for (ii) we are interested in the effect of pupil dilation on the
606 ROA density rise rate, as well as the interaction between this pupil effect and the genotype. In both of
607 these sets of analyses we adjusted for the following fixed effect covariates: the level of optical zoom
608 (2 levels), the depth of the measurements (in μm) and the maximal speed in the relevant time window.
609 We included random intercepts for each mouse (5 WT and 6 tg-ArcSwe). We analyzed the ROA
610 density max and mean values with similar models as the ones described here for the rise rate. For (i),
611 the number of observations ranged between 77 to 117 trials with startle data (depending on the
612 subcompartment) and between 72 and 109 episodes of spontaneous running, while for (ii) the number
613 of observations ranged between 60 and 86 for the startle data and between 35 and 44 for the
614 spontaneous runs. There were less observations for the (ii) analyses because some episodes/trials had
615 missing or incomplete pupil measurements.

616

617 The sensitivity of our result to these modelling choices were assessed by various robustness checks,
618 see next section. The adequacy of model assumptions was investigated by residual plots (Hartig,
619 n.d.). In the cases where the residual plots indicated deviations from the assumption of constant
620 residual variance, we extended the model by allowing the residual variance to vary as a function of
621 genotype. The reported p-values are based on the t-distribution, with degrees of freedom as provided
622 from the glmmTMB package. No corrections for multiple comparisons were applied.

623

624 When analysing the relationship between distance from the nearest plaque and astrocytic Ca^{2+}
625 signalling (Figure 1E) we considered the mean ROA density in each ROI ($n=10988$) in the quiet
626 wakefulness episodes. If present, any effect of plaque proximity on Ca^{2+} signalling should be
627 discernible among ROIs observed in the same episode. The dashed lines in Figure 1E show the effect
628 of distance on Ca^{2+} signalling within each episode, and they form an uncertain picture: in some
629 episodes there is a weak positive relationship, with seemingly higher mean ROA density further away
630 from plaques, while in many episodes there is a negative relationship, with somewhat higher mean
631 ROA density close to plaques. The overall line is found by fitting a linear mixed effect model with
632 mean ROA density as the response, with a fixed effect of distance and with each episode having its
633 own random intercept and slope for the distance effect.

634

635 For the results presented in Figure 4: Unless otherwise stated, the data are presented as mean \pm
636 standard error of the mean (SEM). A p-value equal to or below 0.05 was considered statistically
637 significant. Mann-Whitney U-test was used to analyse the number of processes, total length of
638 processes in μm , process thickness in μm^3 and area fraction of positive GFAP staining. Two-way
639 ANOVA followed by Sidak post hoc comparison was used to analyse the number of intersections.
640 Statistical analysis was performed in GraphPad Prism version 8.0.1 for Windows (GraphPad
641 Software). For qPCR analysis, mean copy number per ng of total RNA was compared between
642 genotypes by Mann-Whitney U test in SPSS Statistics 26 (SPSS).

643

644 Robustness checks

645 In order to check the robustness of the various statistical analyses, the stability of estimates and p-
646 values was examined with respect to the length of window, for the rise rate response variable, and also
647 sensitivity to individual mice and trials.

648

649 The type of sensitivity analysis performed is illustrated (see Supplementary Figure 6) for the analysis
650 of the uncoupling between pupil dilation and astrocytic Ca^{2+} responses (see Figure 3 for details about
651 the data). Again, for the purpose of illustration, we focus on the interaction between pupil dilation
652 and genotype for the ROA density rise rate response variable; see Supplementary Figure 6 for details.
653 Similar analyses were performed for the main statistical models, none of these sensitivity analyses
654 provided clear or strong evidence for any change in the main conclusions.

655

656 Data and source code availability

657 A complete dataset of raw and processed data including Ca²⁺ signal traces, behavioral monitoring
658 traces (all sampled and time aligned to 30Hz) and pupil tracking data are provided at:

659 <https://doi.org/10.11582/2021.00100>. Data analyses were performed with the Begonia toolkit

660 (Bjørnstad et al. 2021), which is available at <https://github.com/GliaLab/Begonia>.

661

662 Acknowledgements

663 This work was supported by the Olav Thon Foundation, the Letten Foundation, Norwegian Health
664 Association, Alzheimer fond, the Research Council of Norway (grants #249988), the South-Eastern
665 Norway Regional Health Authority (grant #2016070). We acknowledge the support by UNINETT
666 Sigma2 AS for making data storage available through NIRD, project NS9021K. Prof. Lars Lannfelt is
667 gratefully acknowledged for help to the development of the tg-ArcSwe mouse model at Uppsala
668 University.

669

670 Author contributions

671 Conceptualization: E.A.N., R.T., R.E.; Methodology: K.S.Å., G.H.E.S.S., D.M.B., R.T., R.E., V.J.,
672 W.T., L.N.G.N; S.B.R. Software: K.S.Å., D.M.B., R.E., C.C., G.H.H.; Formal analysis: K.S.Å.,
673 G.H.E.S.S., R.E., C.C., G.H.H.; Investigation: L.B.; Resources: W.T., E.A.N., R.T., R.E.; Writing—
674 original draft: O.O., R.E., K.S.Å., G.H.E.S.S.; Writing—review and editing: O.O., K.S.Å.,
675 G.H.E.S.S., R.T., D.M.B., C.C., G.H.H., K.M.G.B., V.J., L.N.G.N; Visualization: K.S.Å., G.H.E.S.S.,
676 R.E.; Supervision: R.E., E.A.N., V.J., R.T.; Funding acquisition: E.A.N., R.E., R.T.

677 References

- 678 Abramov, Andrey Y., Laura Canevari, and Michael R. Duchen. 2003. “Changes in Intracellular
679 Calcium and Glutathione in Astrocytes as the Primary Mechanism of Amyloid Neurotoxicity.”
680 *The Journal of Neuroscience: The Official Journal of the Society for Neuroscience* 23 (12):
681 5088–95.
- 682 Abramov, Andrey Y., Laura Canevari, and Michael R. Duchen. 2004. “Calcium Signals Induced by
683 Amyloid β Peptide and Their Consequences in Neurons and Astrocytes in Culture.” *Biochimica*
684 *et Biophysica Acta (BBA) - Molecular Cell Research* 1742 (1): 81–87.
- 685 Adamsky, Adar, Adi Kol, Tirzah Kreisel, Adi Doron, Nofar Ozeri-Engelhard, Talia Melcer, Ron
686 Refaeli, et al. 2018. “Astrocytic Activation Generates De Novo Neuronal Potentiation and
687 Memory Enhancement.” *Cell* 174 (1): 59–71.e14.
- 688 Bekar, Lane K., Wei He, and Maiken Nedergaard. 2008. “Locus Coeruleus α -Adrenergic-Mediated
689 Activation of Cortical Astrocytes In Vivo.” *Cerebral Cortex* 18 (12): 2789–95.
- 690 Bindocci, Erika, Iaroslav Savtchouk, Nicolas Liaudet, Denise Becker, Giovanni Carriero, and Andrea

- 691 Volterra. 2017. “Three-Dimensional Ca²⁺ Imaging Advances Understanding of Astrocyte
692 Biology.” *Science* 356 (6339).
- 693 Bjørnstad, Daniel M., Knut S. Åbjørsbråten, Eivind Hennestad, Céline Cunen, Gudmund Horn
694 Hermansen, Laura Bojarskaite, Klas H. Pettersen, Koen Vervaeke, and Rune Enger. 2021.
695 “Begonia—A Two-Photon Imaging Analysis Pipeline for Astrocytic Ca²⁺ Signals.” *Frontiers in*
696 *Cellular Neuroscience* 15: 176.
- 697 Bojarskaite, Laura, Daniel M. Bjørnstad, Klas H. Pettersen, Céline Cunen, Gudmund Horn
698 Hermansen, Knut Sindre Åbjørsbråten, Anna R. Chambers, et al. 2020. “Astrocytic Ca²⁺
699 Signaling Is Reduced during Sleep and Is Involved in the Regulation of Slow Wave Sleep.”
700 *Nature Communications* 11 (1): 1–16.
- 701 Braak, Heiko, and Kelly Del Tredici. 2011. “The Pathological Process Underlying Alzheimer’s
702 Disease in Individuals under Thirty.” *Acta Neuropathologica* 121 (2): 171–81.
- 703 Brooks, M. E., K. Kristensen, and K. J. Van Benthem. 2017. “glmmTMB Balances Speed and
704 Flexibility among Packages for Zero-Inflated Generalized Linear Mixed Modeling.” *The R*.
705 <https://www.research-collection.ethz.ch/handle/20.500.11850/239870>.
- 706 Caggiano, V., R. Leiras, H. Goñi-Erro, D. Masini, C. Bellardita, J. Bouvier, V. Caldeira, G. Fisone,
707 and O. Kiehn. 2018. “Midbrain Circuits That Set Locomotor Speed and Gait Selection.” *Nature*
708 553 (7689): 455–60.
- 709 Chen, Tsai-Wen, Trevor J. Wardill, Yi Sun, Stefan R. Pulver, Sabine L. Renninger, Amy Baohan,
710 Eric R. Schreiter, et al. 2013. “Ultrasensitive Fluorescent Proteins for Imaging Neuronal
711 Activity.” *Nature* 499 (7458): 295–300.
- 712 Codita, Alina, Astrid Gumucio, Lars Lannfelt, Pär Gellerfors, Bengt Winblad, Abdul H. Mohammed,
713 and Lars N. G. Nilsson. 2010. “Impaired Behavior of Female Tg-ArcSwe APP Mice in the
714 IntelliCage: A Longitudinal Study.” *Behavioural Brain Research* 215 (1): 83–94.
- 715 Costa, Vincent D., and Peter H. Rudebeck. 2016. “More than Meets the Eye: The Relationship
716 between Pupil Size and Locus Coeruleus Activity.” *Neuron*.
- 717 Delekate, Andrea, Martina Füchtmeier, Toni Schumacher, Cordula Ulbrich, Marco Foddis, and
718 Gabor C. Petzold. 2014. “Metabotropic P2Y₁ Receptor Signalling Mediates Astrocytic
719 Hyperactivity in Vivo in an Alzheimer’s Disease Mouse Model.” *Nature Communications* 5
720 (November): 5422.
- 721 Ding, Fengfei, John O’Donnell, Alexander S. Thrane, Douglas Zeppenfeld, Hongyi Kang, Lulu Xie,
722 Fushun Wang, and Maiken Nedergaard. 2013. “ α 1-Adrenergic Receptors Mediate Coordinated
723 Ca²⁺ Signaling of Cortical Astrocytes in Awake, Behaving Mice.” *Cell Calcium*.
- 724 Escartin, Carole, Elena Galea, András Lakatos, James P. O’Callaghan, Gabor C. Petzold, Alberto
725 Serrano-Pozo, Christian Steinhäuser, et al. 2021. “Reactive Astrocyte Nomenclature, Definitions,
726 and Future Directions.” *Nature Neuroscience* 24 (3): 312–25.
- 727 Ferreira-Pinto, Manuel J., Ludwig Ruder, Paolo Capelli, and Silvia Arber. 2018. “Connecting Circuits
728 for Supraspinal Control of Locomotion.” *Neuron* 100 (2): 361–74.
- 729 Grillner, Sten, and Abdeljabbar El Manira. 2020. “Current Principles of Motor Control, with Special
730 Reference to Vertebrate Locomotion.” *Physiological Reviews* 100 (1): 271–320.
- 731 Habib, Naomi, Cristin McCabe, Sedi Medina, Miriam Varshavsky, Daniel Kitsberg, Raz Dvir-
732 Sztternfeld, Gilad Green, et al. 2020. “Disease-Associated Astrocytes in Alzheimer’s Disease and
733 Aging.” *Nature Neuroscience* 23 (6): 701–6.
- 734 Hancock, M. B., and C. L. Fougere. 1976. “Spinal Projections from the Nucleus Locus Coeruleus
735 and Nucleus Subcoeruleus in the Cat and Monkey as Demonstrated by the Retrograde Transport
736 of Horseradish Peroxidase.” *Brain Research Bulletin* 1 (2): 229–34.
- 737 Hartig, Florian. n.d. “DHARMA: Residual Diagnostics for Hierarchical (Multi-Level / Mixed)
738 Regression Models.” <https://CRAN.R-project.org/package=DHARMA>.
- 739 Haughey, Norman J., and Mark P. Mattson. 2003. “Alzheimer’s Amyloid Beta-Peptide Enhances
740 ATP/gap Junction-Mediated Calcium-Wave Propagation in Astrocytes.” *Neuromolecular*
741 *Medicine* 3 (3): 173–80.
- 742 Haydon, Philip G., and Maiken Nedergaard. 2014. “How Do Astrocytes Participate in Neural
743 Plasticity?” *Cold Spring Harbor Perspectives in Biology* 7 (3): a020438.
- 744 Hirrlinger, Johannes, Anja Scheller, Petra G. Hirrlinger, Beate Kellert, Wannan Tang, Michael C.
745 Wehr, Sandra Goebbels, et al. 2009. “Split-Cre Complementation Indicates Coincident Activity

- 746 of Different Genes in Vivo.” *PloS One* 4 (1): e4286.
- 747 Holland, Negin, Trevor W. Robbins, and James B. Rowe. 2021. “The Role of Noradrenaline in
748 Cognition and Cognitive Disorders.” *Brain: A Journal of Neurology*, March.
749 <https://doi.org/10.1093/brain/awab111>.
- 750 Jacobs, Heidi I. L., John A. Becker, Kenneth Kwong, Nina Engels-Domínguez, Prokopis C.
751 Prokopiou, Kathryn V. Papp, Michael Properzi, et al. 2021. “In Vivo and Neuropathology Data
752 Support Locus Coeruleus Integrity as Indicator of Alzheimer’s Disease Pathology and Cognitive
753 Decline.” *Science Translational Medicine* 13 (612): eabj2511.
- 754 Kjaerby, Celia, Rune Rasmussen, Mie Andersen, and Maiken Nedergaard. 2017. “Does Global
755 Astrocytic Calcium Signaling Participate in Awake Brain State Transitions and Neuronal Circuit
756 Function?” *Neurochemical Research* 42 (6): 1810–22.
- 757 Klunk, William E., Brian J. Bacskai, Chester A. Mathis, Stephen T. Kajdasz, Megan E. McLellan,
758 Matthew P. Frosch, Manik L. Debnath, Daniel P. Holt, Yanming Wang, and Bradley T. Hyman.
759 2002. “Imaging A β Plaques in Living Transgenic Mice with Multiphoton Microscopy and
760 Methoxy-X04, a Systemically Administered Congo Red Derivative.” *Journal of Neuropathology
761 and Experimental Neurology* 61 (9): 797–805.
- 762 Kol, Adi, Adar Adamsky, Maya Groysman, Tirzah Kreisel, Michael London, and Inbal Goshen. 2020.
763 “Astrocytes Contribute to Remote Memory Formation by Modulating Hippocampal–cortical
764 Communication during Learning.” *Nature Neuroscience* 23 (10): 1229–39.
- 765 Kuchibhotla, Kishore V., Carli R. Lattarulo, Bradley T. Hyman, and Brian J. Bacskai. 2009.
766 “Synchronous Hyperactivity and Intercellular Calcium Waves in Astrocytes in Alzheimer Mice.”
767 *Science* 323 (5918): 1211–15.
- 768 Lillehaug, Sveinung, Gry H. Syverstad, Lars N. G. Nilsson, Jan G. Bjaalie, Trygve B. Leergaard, and
769 Reidun Torp. 2014. “Brainwide Distribution and Variance of Amyloid-Beta Deposits in Tg-
770 ArcSwe Mice.” *Neurobiology of Aging* 35 (3): 556–64.
- 771 Lim, Dmitry, Anand Iyer, Virginia Ronco, Ambra A. Grolla, Pier Luigi Canonico, Eleonora Aronica,
772 and Armando A. Genazzani. 2013. “Amyloid Beta Deregulates Astroglial mGluR5-Mediated
773 Calcium Signaling via Calcineurin and Nf-kB.” *Glia*. <https://doi.org/10.1002/glia.22502>.
- 774 Liu, Yang, Charles Rodenkirch, Nicole Moskowitz, Brian Schriver, and Qi Wang. 2017. “Dynamic
775 Lateralization of Pupil Dilation Evoked by Locus Coeruleus Activation Results from
776 Sympathetic, Not Parasympathetic, Contributions.” *Cell Reports* 20 (13): 3099–3112.
- 777 Longair, Mark H., Dean A. Baker, and J. Douglas Armstrong. 2011. “Simple Neurite Tracer: Open
778 Source Software for Reconstruction, Visualization and Analysis of Neuronal Processes.”
779 *Bioinformatics* 27 (17): 2453–54.
- 780 Lord, Anna, Hannu Kalimo, Chris Eckman, Xiao-Qun Zhang, Lars Lannfelt, and Lars N. G. Nilsson.
781 2006. “The Arctic Alzheimer Mutation Facilitates Early Intraneuronal A β Aggregation and
782 Senile Plaque Formation in Transgenic Mice.” *Neurobiology of Aging* 27 (1): 67–77.
- 783 McCool, Martha F., Geoffrey B. Varty, Robert A. Del Vecchio, Tatiana M. Kazdoba, Eric M. Parker,
784 John C. Hunter, and Lynn A. Hyde. 2003. “Increased Auditory Startle Response and Reduced
785 Prepulse Inhibition of Startle in Transgenic Mice Expressing a Double Mutant Form of Amyloid
786 Precursor Protein.” *Brain Research* 994 (1): 99–106.
- 787 Meyer-Luehmann, Melanie, Tara L. Spires-Jones, Claudia Prada, Monica Garcia-Alloza, Alix de
788 Calignon, Anete Rozkalne, Jessica Koenigsnecht-Talboo, David M. Holtzman, Brian J.
789 Bacskai, and Bradley T. Hyman. 2008. “Rapid Appearance and Local Toxicity of Amyloid-Beta
790 Plaques in a Mouse Model of Alzheimer’s Disease.” *Nature* 451 (7179): 720–24.
- 791 Paukert, Martin, Amit Agarwal, Jaepyeong Cha, Van A. Doze, Jin U. Kang, and Dwight E. Bergles.
792 2014. “Norepinephrine Controls Astroglial Responsiveness to Local Circuit Activity.” *Neuron*
793 82 (6): 1263–70.
- 794 Peterson, Andrew C., and Chiang-Shan R. Li. 2018. “Noradrenergic Dysfunction in Alzheimer’s and
795 Parkinson’s Diseases—An Overview of Imaging Studies.” *Frontiers in Aging Neuroscience* 10:
796 127.
- 797 Philipson, Ola, Per Hammarström, K. Peter R. Nilsson, Erik Portelius, Tommie Olofsson, Martin
798 Ingelsson, Bradley T. Hyman, et al. 2009. “A Highly Insoluble State of A β Similar to that of
799 Alzheimer’s Disease Brain Is Found in Arctic APP Transgenic Mice.” *Neurobiology of Aging* 30
800 (9): 1393–1405.

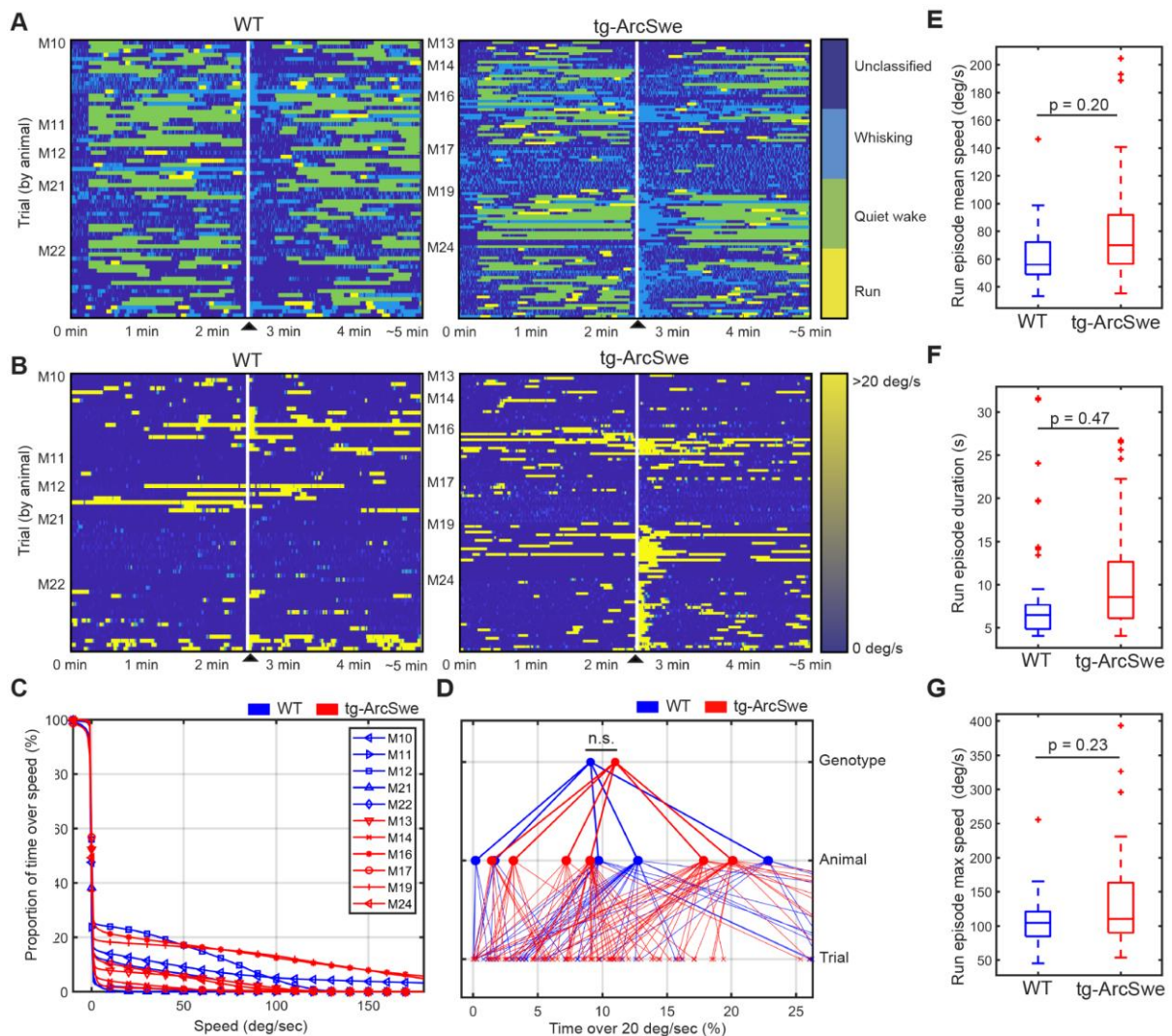
- 801 Poskanzer, Kira E., and Rafael Yuste. 2011. "Astrocytic Regulation of Cortical UP States."
802 *Proceedings of the National Academy of Sciences of the United States of America* 108 (45):
803 18453–58.
- 804 Poskanzer, Kira E., and Rafael Yuste. 2016. "Astrocytes Regulate Cortical State Switching in Vivo."
805 *Proceedings of the National Academy of Sciences of the United States of America* 113 (19):
806 E2675–84.
- 807 Rao, Shreyas B., Nadia Skauli, Nenad Jovanovic, Shirin Katozi, Antonio Frigeri, Stanley C.
808 Froehner, Marvin E. Adams, Ole Petter Ottersen, and Mahmood Amiry-Moghaddam. 2021.
809 "Orchestrating Aquaporin-4 and Connexin-43 Expression in Brain: Differential Roles of $\alpha 1$ - and
810 $\beta 1$ -Syntrophin." *Biochimica et Biophysica Acta, Biomembranes* 1863 (8): 183616.
- 811 Reimer, Jacob, Matthew J. McGinley, Yang Liu, Charles Rodenkirch, Qi Wang, David A.
812 McCormick, and Andreas S. Tolias. 2016. "Pupil Fluctuations Track Rapid Changes in
813 Adrenergic and Cholinergic Activity in Cortex." *Nature Communications* 7 (November): 13289.
- 814 Rodríguez-Arellano, J. J., V. Parpura, R. Zorec, and A. Verkhratsky. 2016. "Astrocytes in
815 Physiological Aging and Alzheimer's Disease." *Neuroscience*.
816 <https://doi.org/10.1016/j.neuroscience.2015.01.007>.
- 817 Sano, Fumikazu, Eiji Shigetomi, Youichi Shinozaki, Haruka Tsuzuki-yama, Kozo Saito, Katsuhiko
818 Mikoshiba, Kanji Sugita, Masao Aihara, and Schuichi Koizumi. n.d. "Reactive Astrocyte-Driven
819 Epileptogenesis Is Induced by Microglia Initially Activated Following Status Epilepticus."
820 <https://doi.org/10.1101/806398>.
- 821 Schindelin, Johannes, Ignacio Arganda-Carreras, Erwin Frise, Verena Kaynig, Mark Longair, Tobias
822 Pietzsch, Stephan Preibisch, et al. 2012. "Fiji: An Open-Source Platform for Biological-Image
823 Analysis." *Nature Methods* 9 (7): 676–82.
- 824 Shevtsova, Z., J. M. I. Malik, U. Michel, M. Bähr, and S. Kügler. 2005. "Promoters and Serotypes:
825 Targeting of Adeno-Associated Virus Vectors for Gene Transfer in the Rat Central Nervous
826 System in Vivo." *Experimental Physiology*.
827 <https://doi.org/10.1113/expphysiol.2004.028159>.
- 828 Shigetomi, Eiji, Kozo Saito, Fumikazu Sano, and Schuichi Koizumi. 2019. "Aberrant Calcium
829 Signals in Reactive Astrocytes: A Key Process in Neurological Disorders." *International Journal*
830 *of Molecular Sciences* 20 (4). <https://doi.org/10.3390/ijms20040996>.
- 831 Smith, Richard H., Justin R. Levy, and Robert M. Kotin. 2009. "A Simplified Baculovirus-AAV
832 Expression Vector System Coupled with One-Step Affinity Purification Yields High-Titer rAAV
833 Stocks from Insect Cells." *Molecular Therapy: The Journal of the American Society of Gene*
834 *Therapy* 17 (11): 1888–96.
- 835 Srinivasan, Rahul, Ben S. Huang, Sharmila Venugopal, April D. Johnston, Hua Chai, Hongkui Zeng,
836 Peyman Golshani, and Baljit S. Khakh. 2015. "Ca²⁺ Signaling in Astrocytes from *Ip3r2*^{-/-} Mice in
837 Brain Slices and during Startle Responses in Vivo." *Nature Neuroscience* 18 (5): 708–17.
- 838 Stobart, Jillian L., Kim David Ferrari, Matthew J. P. Barrett, Chaim Glück, Michael J. Stobart, Marc
839 Zuend, and Bruno Weber. 2018. "Cortical Circuit Activity Evokes Rapid Astrocyte Calcium
840 Signals on a Similar Timescale to Neurons." *Neuron* 98 (4): 726–35.e4.
- 841 Syverstad Skaaraas, Gry H. E., Christoffer Melbye, Maja A. Puchades, Doreen Siu Yi Leung, Øyvind
842 Jacobsen, Shreyas B. Rao, Ole Petter Ottersen, Trygve B. Leergaard, and Reidun Torp. 2021.
843 "Cerebral Amyloid Angiopathy in a Mouse Model of Alzheimer's Disease Associates with
844 Upregulated Angiopoietin and Downregulated Hypoxia-Inducible Factor." *Journal of*
845 *Alzheimer's Disease: JAD Preprint*: 1–13.
- 846 Tang, W., K. Szokol, V. Jensen, and R. Enger. 2015. "Stimulation-Evoked Ca²⁺ Signals in Astrocytic
847 Processes at Hippocampal CA3–CA1 Synapses of Adult Mice Are Modulated by Glutamate and
848 ATP." *Journal of*. <https://www.jneurosci.org/content/35/7/3016.short>.
- 849 Tavares, Gabriela, Manuella Martins, Joana Sofia Correia, Vanessa Morais Sardinha, Sónia Guerra-
850 Gomes, Sofia Pereira das Neves, Fernanda Marques, Nuno Sousa, and João Filipe Oliveira.
851 2017. "Employing an Open-Source Tool to Assess Astrocyte Tridimensional Structure." *Brain*
852 *Structure & Function* 222 (4): 1989–99.
- 853 Thrane, Alexander Stanley, Vinita Rangroo Thrane, Douglas Zeppenfeld, Nanhong Lou, Qiwu Xu,
854 Erlend Arnulf Nagelhus, and Maiken Nedergaard. 2012. "General Anesthesia Selectively
855 Disrupts Astrocyte Calcium Signaling in the Awake Mouse Cortex." *Proceedings of the National*

- 856 *Academy of Sciences of the United States of America* 109 (46): 18974–79.
- 857 Vaidyanathan, Trisha V., Max Collard, Sae Yokoyama, Michael E. Reitman, and Kira E. Poskanzer.
- 858 2021. “Cortical Astrocytes Independently Regulate Sleep Depth and Duration via Separate
- 859 GPCR Pathways.” *eLife* 10 (March). <https://doi.org/10.7554/eLife.63329>.
- 860 Verkhratsky, Alexei. 2019. “Astroglial Calcium Signaling in Aging and Alzheimer’s Disease.” *Cold*
- 861 *Spring Harbor Perspectives in Biology* 11 (7). <https://doi.org/10.1101/cshperspect.a035188>.
- 862 Wang, Fushun, Nathan A. Smith, Qiwu Xu, Takumi Fujita, Akemichi Baba, Toshio Matsuda,
- 863 Takahiro Takano, Lane Bekar, and Maiken Nedergaard. 2012. “Astrocytes Modulate Neural
- 864 Network Activity by Ca²⁺-Dependent Uptake of Extracellular K⁺.” *Science Signaling* 5 (218):
- 865 ra26–ra26.
- 866 Wang, Yizhi, Nicole V. DelRosso, Trisha V. Vaidyanathan, Michelle K. Cahill, Michael E. Reitman,
- 867 Silvia Pittolo, Xuelong Mi, Guoqiang Yu, and Kira E. Poskanzer. 2019. “Accurate
- 868 Quantification of Astrocyte and Neurotransmitter Fluorescence Dynamics for Single-Cell and
- 869 Population-Level Physiology.” *Nature Neuroscience* 22 (11): 1936–44.
- 870 Weinshenker, David. 2018. “Long Road to Ruin: Noradrenergic Dysfunction in Neurodegenerative
- 871 Disease.” *Trends in Neurosciences* 41 (4): 211–23.
- 872 Wilhelmsson, Ulrika, Eric A. Bushong, Diana L. Price, Benjamin L. Smarr, Van Phung, Masako
- 873 Terada, Mark H. Ellisman, and Milos Pekny. 2006. “Redefining the Concept of Reactive
- 874 Astrocytes as Cells That Remain within Their Unique Domains upon Reaction to Injury.”
- 875 *Proceedings of the National Academy of Sciences of the United States of America* 103 (46):
- 876 17513–18.
- 877 Yang, Jing, Lisa K. Lunde, Paworn Nuntagij, Tomohiro Oguchi, Laura M. A. Camassa, Lars N. G.
- 878 Nilsson, Lars Lannfelt, et al. 2011. “Loss of Astrocyte Polarization in the Tg-ArcSwe Mouse
- 879 Model of Alzheimer’s Disease.” *Journal of Alzheimer’s Disease: JAD* 27 (4): 711–22.
- 880 Ye, Liang, Murat Orynbayev, Xiangyu Zhu, Eunice Y. Lim, Ram R. Dereddi, Amit Agarwal, Dwight
- 881 E. Bergles, Manzoor A. Bhat, and Martin Paukert. 2020. “Ethanol Abolishes Vigilance-
- 882 Dependent Astroglia Network Activation in Mice by Inhibiting Norepinephrine Release.” *Nature*
- 883 *Communications* 11 (1): 1–20.
- 884 Yüzgeç, Özge, Mario Prsa, Robert Zimmermann, and Daniel Huber. 2018. “Pupil Size Coupling to
- 885 Cortical States Protects the Stability of Deep Sleep via Parasympathetic Modulation.” *Current*
- 886 *Biology: CB* 28 (3): 392–400.e3.
- 887 Zuend, Marc, Aiman S. Saab, Matthias T. Wyss, Kim David Ferrari, Ladina Hösli, Zoe J. Looser,
- 888 Jillian L. Stobart, et al. 2020. “Arousal-Induced Cortical Activity Triggers Lactate Release from
- 889 Astrocytes.” *Nature Metabolism* 2 (2): 179–91.

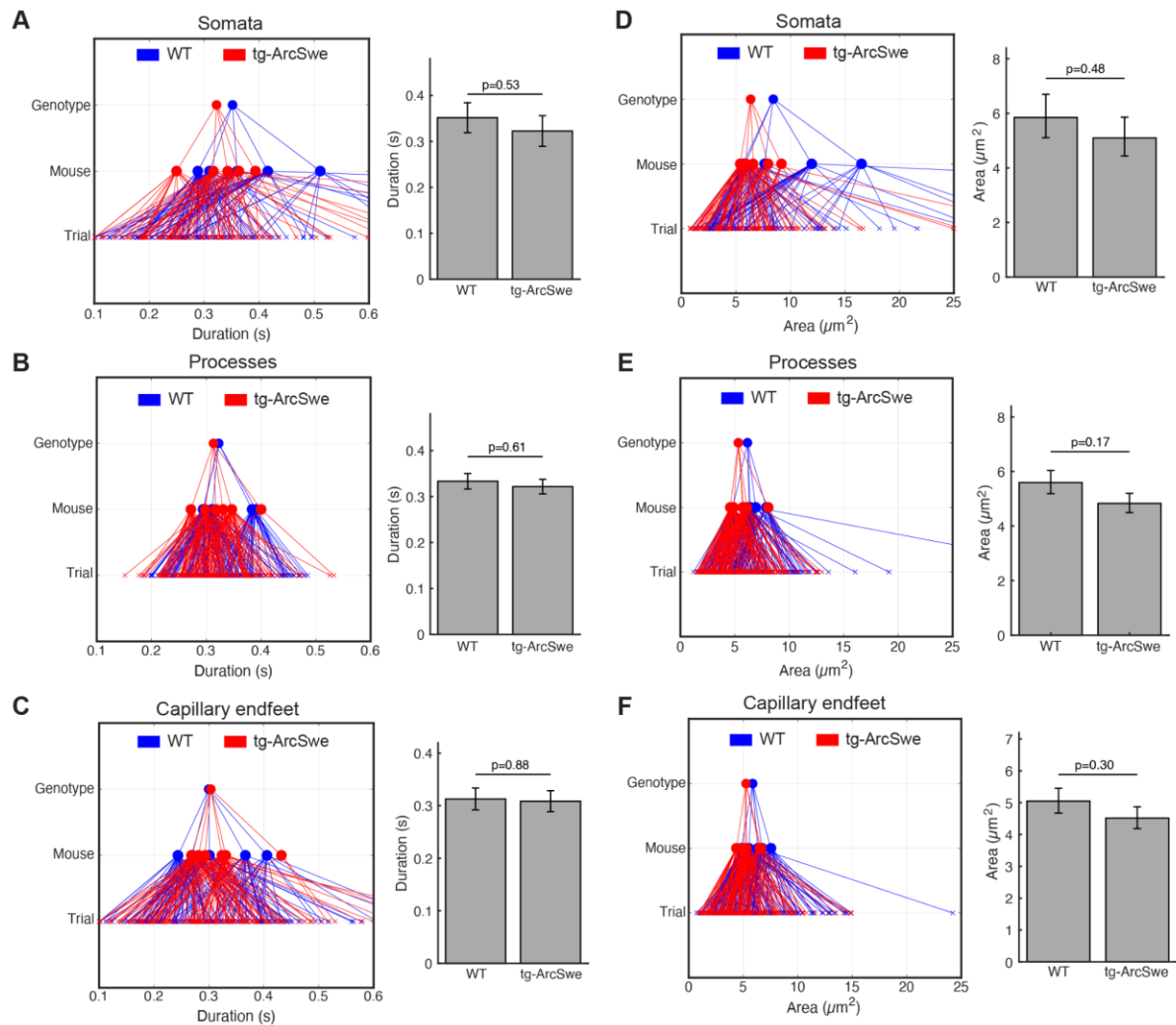
Supplementary Information for

Impaired astrocytic Ca²⁺ signalling in awake Alzheimer's disease transgenic mice

Åbjørsbråten et al.

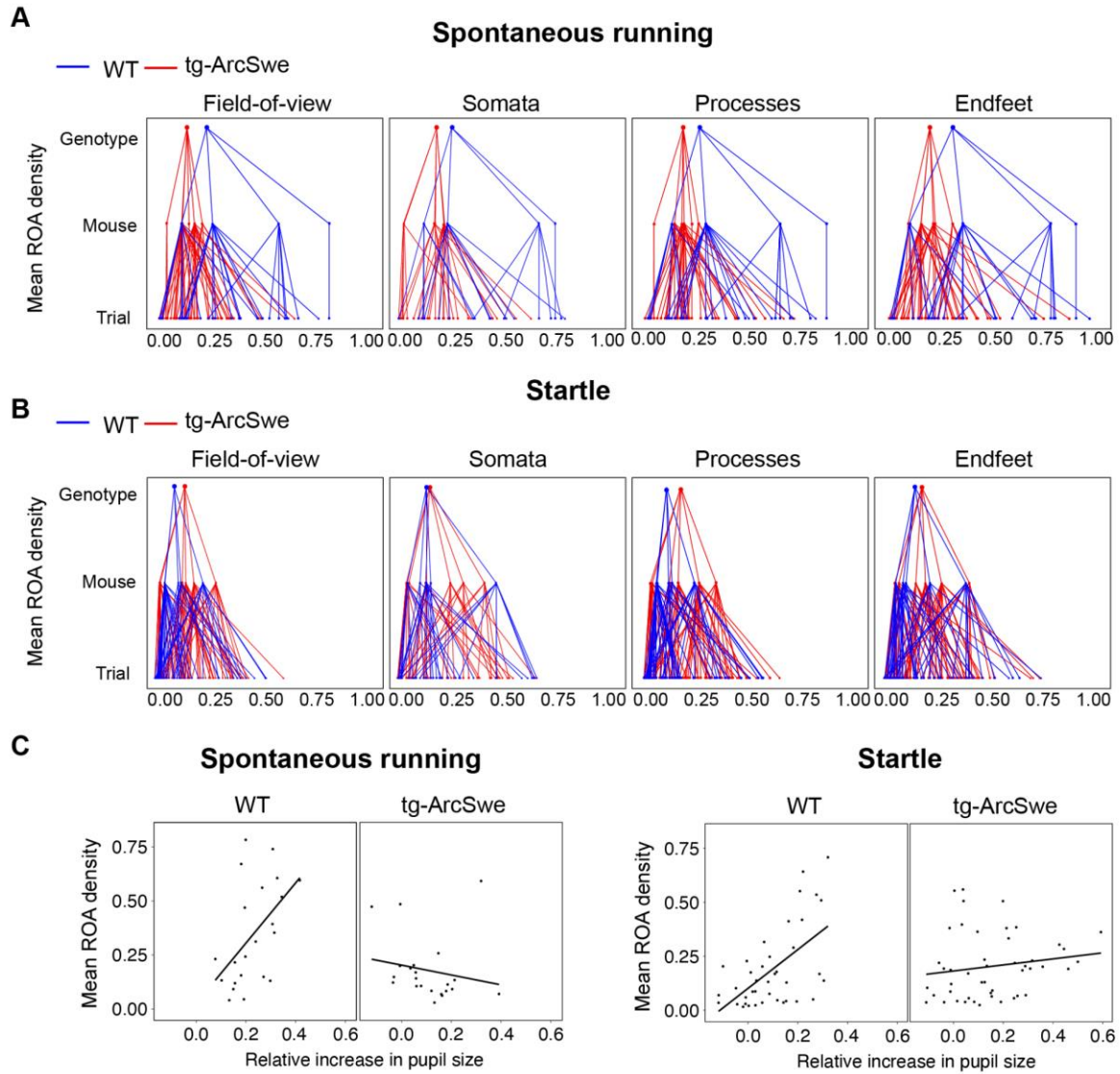


Supplementary Figure 1. Locomotor behavior in WT and tg-ArcSwe mice. ▲ indicates air-puff. (A) Behavioral classification for each individual trial, grouped by mouse. See methods for classification and filtering algorithm used. (B) Running wheel speed for each individual trial, grouped by mouse. 20 degrees of rotation of the running wheel per s was the threshold used to classify running. (C) Percentage of total time a mouse spent above a given speed across all trials. (D) Percentage of total time a mouse was running (> 20 degrees/s). Raw running data not filtered by the run classification algorithm ($p = 0.35$). (E, F, G) Post-classification run episode characteristics.

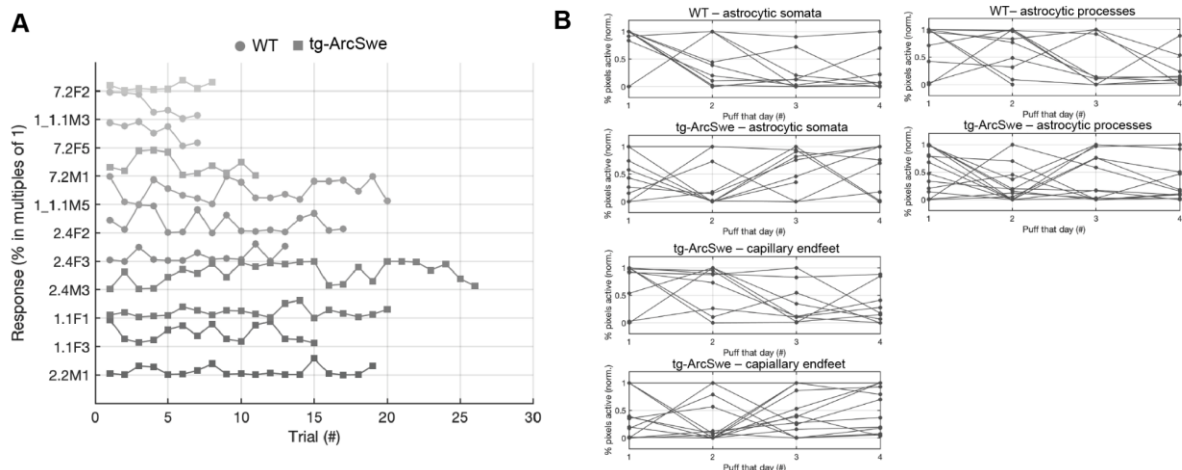


Supplementary Figure 2. Regions-of-Activity during quiet wakefulness exhibit the same characteristics in both genotypes. During quiet wakefulness episodes, active regions detected by the ROA algorithm. Compartment association is determined by the centre of the region-of-activity. (A, B, C) Mean duration of active regions during quiet wakefulness in different cellular compartments. Right: GLME statistical analysis estimates. (D, E, F) Mean maximum size of a detected region. Right: GLME statistical analysis estimates.

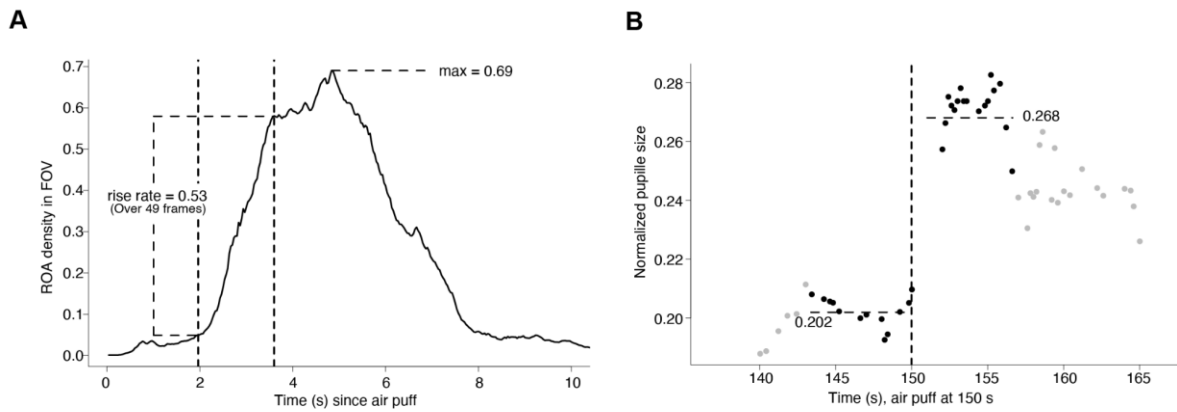
Supplementary Figure 3. (A) Hierarchical showing medians of mean ROA density per trial, mouse and genotype in the FOV and astrocytic subcellular compartments during spontaneous runs. (B) Same as (A) but during startle responses. (C) Scatterplots of mean ROA density vs. relative increase in pupil size in



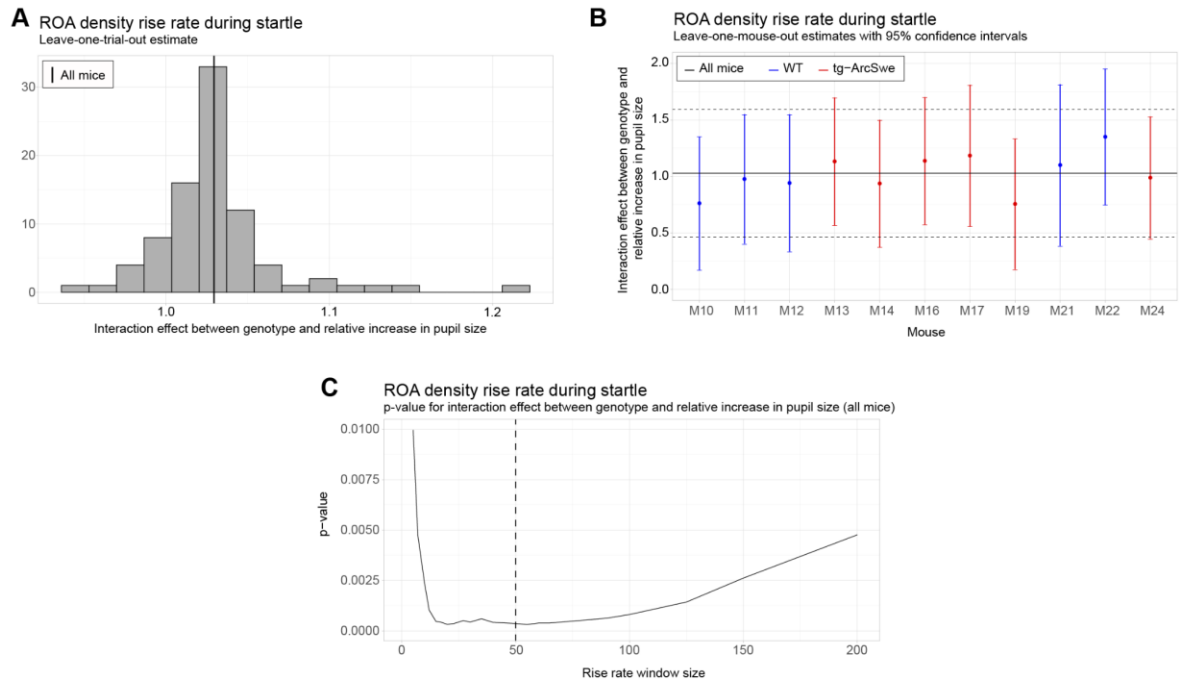
spontaneous running and startle responses.



Supplementary Figure 4. (A) Neither tg-ArcSwe or WT mice displayed any noticeable habituation to air puffs across all trials and experimental days. (B) Within a single experimental day, there was no habituation to air puffs across the different trials.



Supplementary Figure 5. (A) Computation of the ROA density rise rate, and max ROA density, in particular startle period. The vertical dashed lines indicate the time window which had the maximal increase in ROA density, which in this example took place over 49 frames. (B) Computation of the pupil dilation in a particular startle period, here we find $(0.268-0.202)/0.202=0.33$.



Supplementary Figure 6. Robustness and sensitivity analyses for the uncoupling between pupil dilation and the ROA density rise rate. All analyses are with respect to the interaction effect between pupil dilation and genotype. (A) Leave-one-trial-out analysis. The full model is repeatedly estimated removing one trial at the time from the dataset (as a type of jackknife resampling). The estimated interaction coefficients are shown as a histogram. Note that the histogram indicates less variation in the estimated interaction when comparing the variance or empirical quantiles of the histogram with the corresponding confidence interval obtained from the linear mixed effect model (see solid and dashed lines in Plot B). (B) Leave-one-mouse-out analysis. In each iteration, one mouse, M10-M24, is removed from the estimation of the model. The estimated interaction effects with corresponding confidence intervals are then compared to the estimate and confidence interval from the full model (solid and dashed horizontal lines). Some mice influence the results more than others, but there appears to be no systematic bias associated with a single mouse. (C) The p-value for the interaction effect for different window lengths. The window length is measured in number of frames. It is clear that the significance of the interaction effect does not depend strongly on a particular choice of window length. In the analysis we used a window of length 50 frames.